

Variational system identification of the partial differential equations governing microstructure evolution in materials: Inference over sparse and spatially unrelated data

Z. Wang*, X. Huan[†] and K. Garikipati[‡]

September 27, 2022

Abstract

Pattern formation is a widely observed phenomenon in diverse fields including materials physics, developmental biology and ecology, among many others. The physics underlying the patterns is specific to the mechanisms, and is encoded by partial differential equations (PDEs). With the aim of discovering hidden physics, we have previously presented a variational approach to identifying such systems of PDEs in the face of noisy data at varying fidelities (*Computer Methods in Applied Mechanics and Engineering*, **353**:201-216, 2019). Here, we extend our variational system identification methods to address the challenges presented by image data on microstructures in materials physics. PDEs are formally posed as initial and boundary value problems over combinations of time intervals and spatial domains whose evolution is either fixed or can be tracked. However, the vast majority of microscopy techniques for evolving microstructure in a given material system deliver micrographs of pattern evolution over domains that bear no relation with each other at different time instants. The temporal resolution can rarely capture the fastest time scales that dominate the early dynamics, and noise abounds. Furthermore, data for evolution of the same phenomenon in a material system may well be obtained from different physical specimens. Against this backdrop of spatially unrelated, sparse and multi-source data, we exploit the variational framework to make judicious choices of weighting functions and identify PDE operators from the dynamics. A consistency condition arises for parsimonious inference of a minimal set of the spatial operators at steady state. It is complemented by a confirmation test that provides a sharp condition for acceptance of the inferred operators. The entire framework is demonstrated on synthetic data that reflect the characteristics of the experimental material microscopy images.

*Department of Mechanical Engineering, University of Michigan

[†]Department of Mechanical Engineering, Michigan Institute for Computational Discovery & Engineering, University of Michigan, University of Michigan

[‡]Departments of Mechanical Engineering, and Mathematics, Michigan Institute for Computational Discovery & Engineering, University of Michigan, corresponding author, krishna@umich.edu

1 Introduction

Pattern-formation is ubiquitous in many branches of the physical sciences. It occurs prominently in material microstructures driven by diffusion, reaction and phase transformations, and is revealed by a range of microscopy techniques that delineate the components or constituent phases. In developmental biology, examples include the organization of cells in the early embryo, markings on animal coats, insect wings, plant petals and leaves, as well as the segregation of cell types during the establishment of tissues. In ecology, patterns are formed on larger scales as types of vegetation spreads across forests. For context, we briefly discuss the role of pattern forming systems of equations in these phenomena. Pattern formation during phase transformations in materials physics can happen as the result of instability-induced bifurcations from a uniform composition [1, 2, 3], which was the original setting of the Cahn-Hilliard treatment [4]. Following Alan Turing's seminal work on reaction-diffusion systems [5], a robust literature has developed on the application of nonlinear versions of this class of partial differential equations (PDEs) to model pattern formation in developmental biology [6, 7, 8, 9, 10, 11, 12, 13, 14]. The Cahn-Hilliard phase field equation has also been applied to model other biological processes with evolving fronts, such as tumor growth and angiogenesis [15, 16, 17, 18, 19, 20, 21, 22]. Reaction-diffusion equations also appear in ecology, where they are more commonly referred to as activator-inhibitor systems, and are found to underlie large scale patterning [23, 24]. All of these pattern forming systems fall into the class of nonlinear, parabolic PDEs, and have spawned a vast literature in mathematical physics. They can be written as systems of first-order dynamics driven by a number of time-independent terms of algebraic and differential form. The spatio-temporal, differentio-algebraic operators act on either a composition (normalized concentration) or an order parameter. It also is common for the algebraic and differential terms to be coupled across multiple species.

Patterns in physical systems are of interest because, up to a point, human experts in each of the above fields (materials microscopists, developmental biologists and ecologists) are able to identify phenomena solely on the basis of patterns. This success of intuition fed by experience does, however, break down when, for instance, the materials scientist is confronted by the dynamic processes in an unstudied alloy, or the developmental biologist considers a previously neglected aspect of morphogenesis. In such settings the challenge is to discover the operative physics from among a range of mechanisms. As with all of quantitative physics, the only rigorous route to such discovery is the mathematical one. For systems that vary over space and time, this description is in the form of PDEs. Identification of participating PDE operators from spatio-temporal observations can thus uncover the underlying physical mechanisms, and lead to improved understanding, prediction, and manipulation of these systems.

Distinct from classical adjoint-based approaches to inverse problems, the system identification problem on PDEs is to balance accuracy and complexity in finding the best model among many possible candidates that could explain the spatio-temporal data on the dynamical system. The

proposed models can be parameterized by the coefficients of candidate operators, which serve as a basis. The task of solving this inverse problem can then be posed as finding the best coefficient values that allow a good agreement between model predictions and data. Sparsity of these coefficients is further motivated by the principle that parsimony of physical mechanisms is favored. The comparison procedure between models and data may be set up via the following two broad approaches. (a) When only sparse and noisy data are available, which might also be of indirect quantities that do not explicitly enter the PDEs, quantifying uncertainty in the identification becomes important and a Bayesian statistical approach is very useful. (b) When relatively larger volumes of observed data are accessible for quantities that directly participate in the PDEs, regression-based methods seeking to minimize an appropriate loss function can be highly efficient.

The first (Bayesian) approach has been successfully used for inferring a fixed number of coefficients in specified PDE models, leveraging efficient sampling algorithms such as Markov Chain Monte Carlo [25]. However, they generally require many forward solutions of the PDE models, which is computationally expensive and may quickly become impractical with growth in the number of PDE terms (i.e., dimension of the identification problem). As a result, the use of Bayesian approaches for identifying the best model from a large candidate set remains challenging. If made practical, they can be advantageous in providing uncertainty information, and offering significant flexibility in accommodating the data, which could be sparse and noisy, only available over some subset of the domain, collected at a few time steps, and composed of multiple statistical measures, functionals of the solution, or other indirect Quantities of Interests (QoIs). In the second (regression) approach, the PDEs themselves have to be represented by the data, which can be achieved by constructing the operators either in strong form such as finite difference, as in the Sparse Identification of Nonlinear Dynamics (SINDy) approach [26], or in weak form built upon basis functions, as in the Variational System Identification (VSI) approach [27]. Both representations pose stringent requirements on the data for accurately constructing the operators. The first of these is the need for time series data that can be related to chosen spatial points either directly or by interpolation. This is essential for consistency with a PDE that is written in terms of spatio-temporal operators at defined points in space and instants in time. The second requirement is for data with sufficient spatial resolution to construct spatial differential operators of possibly high order. However, these regression approaches enjoy the advantage over Bayesian methods that repeated forward PDE solutions are not necessary. PDE operators have thus been successfully identified from a comprehensive library of candidates [26, 27, 28, 29]. In a different approach to solving inverse problems [30], the strong form of a specified PDE is directly embedded in the loss function while training deep neural network representations of the solution variable. However, this approach depends on data at high spatial and temporal resolution for successful training of the deep neural network representations of the solution variable. A perspective and comparison between these two approaches can be found in Ref. [31].

A significant discordance can exist in the form of material microstructure datasets when juxtaposed against the underlying premise of all the above approaches. These experimental datasets, while corresponding to different times are also commonly collected over different spatial subdomains of a physical specimen at each instant. This includes scenarios where the spatial subdomains have no overlap and are unrelated to each other. Furthermore, while subject to the same processing conditions, they may well come from different physical specimens. This is because the experimental techniques for extracting data at a given time after specimen preparation (which can include mechanical, chemical and thermal steps) involve destructive processes including cutting and grinding of the specimen. After this procedure, the entire specimen is removed from further experimentation, and a new specimen needs to be created if data is to be collected at a different time. Both of these conditions essentially negate the foundational notion of a PDE describing the temporal evolution of quantities at chosen spatial points for a single instantiation of that initial and boundary value problem (IBVP). The spatial subdomains on which microscopy is conducted may represent only small portions of entire specimens. Boundary data, if present, are also prey to the above loss of spatial localization over time. Finally, the effort of processing (specimen preparation, mechanical, chemical and heat treatment) to attain the desired kinetic rates and thermodynamic driving forces, and subsequently to obtain microscopy images, leads to sparsity of data in time; even tens of instants are uncommon.

In this communication, we extend our VSI methods [27] to sparse and spatially unrelated data, motivated by the above challenges of experimental microscopy in materials physics. The goal remains to discover the physical mechanisms underlying patterns of diffusion, reaction and phase transformation in materials physics. We present novel advances that exploit the variational framework and statistical similarity to circumvent the loss of spatial relatedness so that temporally sparse data prove sufficient for inferring the kinetics. These methods are described in Section 2 and demonstrated on synthetic data in Section 2.5. Furthermore, imposition of consistency on the steady state versions of candidate PDEs opens the door to parsimonious choice of a minimal set of spatial operators. To complement this condition, we also present a confirmation test that is a sharp condition for acceptance of the inferred operators. The confirmation test is described in Section 3 and demonstrated on synthetic data in Section 3.2. Discussions and concluding remarks are presented in Section 4.

2 Variational identification of PDE systems from sparse and spatially unrelated data

2.1 The Galerkin weak form for system identification

We first provide a brief discussion on the weak form of PDEs as used in this work. We start with the general strong form for first-order dynamics written as

$$\frac{\partial C}{\partial t} - \boldsymbol{\chi} \cdot \boldsymbol{\theta} = 0, \quad (1)$$

where $\boldsymbol{\chi}$ is a vector containing all possible linearly independent terms expressed as algebraic and differential operators on the scalar solution C :

$$\boldsymbol{\chi} = [1, C, C^2, \dots, \nabla^2 C, \dots], \quad (2)$$

and $\boldsymbol{\theta}$ is the vector of scalar coefficients of these operators. For example, using this nomenclature, the one-field diffusion reaction equation

$$\frac{\partial C}{\partial t} - D \nabla^2 C - f = 0 \quad (3)$$

with constant diffusivity D and reaction rate f has

$$\boldsymbol{\chi} = [1, C, C^2, \nabla^2 C] \quad \text{and} \quad \boldsymbol{\theta} = [f, 0, 0, D]. \quad (4)$$

Note that the time derivative $\partial C / \partial t$ is treated separately from the other terms in order to highlight the first-order dynamics of the problems that we target in this work. Given some observational data for the dynamical system, our system identification problem entails finding the correct governing equation via the coefficient vector, $\boldsymbol{\theta}$, which specifies the active operators from among a dictionary of candidates, $\boldsymbol{\chi}$.

As argued by Wang et al. [27], the weak form offers particular advantages for the system identification problem. It allows the use of basis functions that can be drawn from function classes that have higher-order regularity. Furthermore, the weak form transfers spatial derivative operators from the trial solution, represented by the data on C , to the weighting function. These two features significantly mollify the noise, stiffness and general loss of robustness associated with constructing spatial derivatives from data. They are especially relevant for the consideration of high-order gradient operators, which are often found in many types of pattern-forming phenomena in physics. Another advantage of writing the PDEs in weak form is that boundary conditions can be constructed as operators, thus making their identification a natural outcome. This weak form approach then leads to what we refer to as Variational System Identification [27], abbreviated here to VSI.

For infinite-dimensional problems with Dirichlet boundary conditions on Γ^c , the weak form is stated as: $\forall w \in \mathcal{V}$ where $\mathcal{V} = \{w \mid w = 0 \text{ on } \Gamma^c\}$, find $C \in \mathcal{S}$ where $\mathcal{S} = \{C \mid C = \bar{C} \text{ on } \Gamma^c\}$ such

that

$$\int_{\Omega} w \left(\frac{\partial C}{\partial t} - \boldsymbol{\chi} \cdot \boldsymbol{\theta} \right) dv = 0. \quad (5)$$

Integration by parts and the application of boundary conditions, which are determined by the operators in $\boldsymbol{\chi}$, leads to the final weak form. In the interest of brevity we have not written out the weak form for each instance of $\boldsymbol{\chi}$. For finite-dimensional fields, C^h and w^h , respectively, replace C and w in the statement of Equation (5): $C^h \in \mathcal{S}^h \subset \mathcal{S}$ where $\mathcal{S}^h = \{C^h \in \mathcal{H}^2(\Omega) \mid C^h = \bar{C} \text{ on } \Gamma^u\}$, and $w^h \in \mathcal{V}^h \subset \mathcal{V}$ where $\mathcal{V}^h = \{w^h \in \mathcal{H}^2(\Omega) \mid w^h = 0 \text{ on } \Gamma^u\}$. The choice of $\mathcal{H}^2(\Omega)$ as the Sobolev space is motivated by the differential operators, which reach the highest order of two in the weak forms we consider (and order four in strong form). The variations w^h and trial solutions C^h are defined component-wise using a finite number of basis functions:

$$w^h = \sum_{a=1}^{n_b} d^a \phi^a \quad (6)$$

$$C^h = \sum_{a=1}^{n_b} c^a \phi^a, \quad (7)$$

where n_b is the dimensionality of the function spaces \mathcal{S}^h and \mathcal{V}^h , and ϕ^a represents the basis functions. Equation (7) represents interpolation of discrete data to obtain fields with regularity specified by \mathcal{H}^2 .

If, at each time instant of interest, t , the data available are in the form $C(\mathbf{x}_I, t)$ such that $\mathbf{x}_I \in \Omega$ for $I = 1, \dots, n_{\text{sp}}$, with n_{sp} being the number of spatial points—that is, if data is available corresponding to discretization points for the entire spatial domain—then VSI [27] presents itself as a powerful approach. However, as explained in the Introduction, the combination of specimen processing and microscopy techniques implies that the data acquired at each time are only available over subdomains of the full field that do not correspond to the same spatial locations—i.e., they are spatially unrelated (Figure 1). For brevity we use the term *snapshot* to refer to the data field over a chosen subdomain and at a given time. Furthermore, each such snapshot is usually produced from a different physical specimen due to the destructive and intrusive nature of data acquisition in the experiments. We next present a two-stage approach that accommodates these scenarios by exploiting the variational setting.

2.2 Two stage variational system identification for dynamics

First, we rewrite Equation (5) as an integral over $\Omega_n \subseteq \Omega$; a subset representing the snapshot over which data was acquired at time t_n . Additionally, we split operators $\boldsymbol{\chi}$ and coefficients $\boldsymbol{\theta}$ into two parts such that $\boldsymbol{\chi} \cdot \boldsymbol{\theta} = \boldsymbol{\chi}_1 \cdot \boldsymbol{\theta}_1 + \boldsymbol{\chi}_2 \cdot \boldsymbol{\theta}_2$. The entire equation is furthermore normalized by

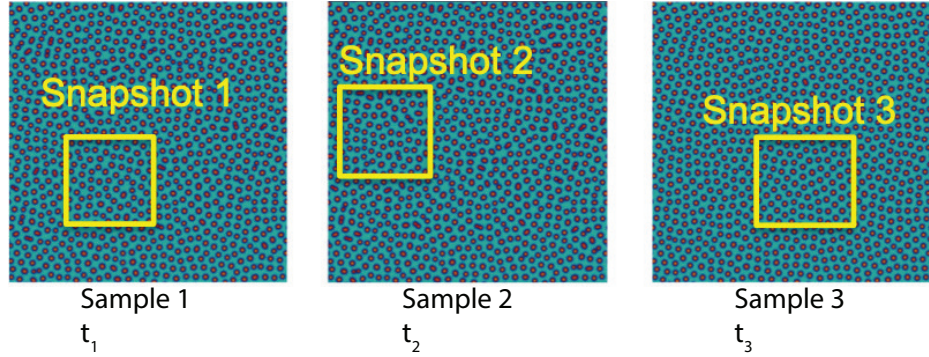


Figure 1: The sample data shown within the snapshots corresponding to each time instant are only available over subdomains of the full field. They are also spatially unrelated over time.

$V_n = \text{vol}(\Omega_n)$. Here, $\text{vol}(\Sigma)$ is the appropriate volume measure on the Euclidean space \mathbb{R}^k if $\Sigma \subset \mathbb{R}^k$ is a k -manifold.

$$\frac{1}{V_n} \int_{\Omega_n} w \left(\frac{\partial C}{\partial t} - (\chi_1 \cdot \theta_1 + \chi_2 \cdot \theta_2) \right) dv = 0. \quad (8)$$

Here, the components of χ_1 contain all the algebraic operators and those of χ_2 contain all the differential operators:

$$\chi_1 = [1, C, C^2, \dots], \quad \chi_2 = [\nabla^2 C, \nabla \cdot C \nabla C, \nabla^4 C, \dots], \quad (9)$$

with θ_1 and θ_2 being the corresponding coefficient vectors. We then use a backward difference approximation of the dynamics, write $\chi_2 \cdot \theta_2$ in divergence form as $\chi_2 \cdot \theta_2 = \nabla \cdot (\hat{\chi}_2 \cdot \hat{\theta}_2)$ and apply integration by parts to arrive at:

$$\frac{1}{V_n} \int_{\Omega_n} w \frac{C_n - C_{n-1}}{\Delta t} dv = \frac{1}{V_n} \left(\int_{\Omega_n} w \chi_{1n} dv \cdot \theta_1 - \int_{\Omega_n} \nabla w \cdot \hat{\chi}_{2n} dv \cdot \hat{\theta}_2 + \int_{\partial \Omega_n} w \hat{\chi}_{2n} \cdot \mathbf{n} ds \cdot \hat{\theta}_2 \right), \quad (10)$$

where $(\bullet)_n$ denotes the time discrete approximation of a field at time t_n .

We define Stage 1 by choosing $w = 1$, yielding:

$$\frac{1}{V_n} \int_{\Omega_n} C_n dv = \frac{1}{V_n} \Delta t \int_{\Omega_n} \chi_{1n} dv \cdot \theta_1 + \frac{1}{V_n} \int_{\Omega_n} C_{n-1} dv + \frac{1}{V_n} \Delta t \int_{\partial \Omega_n} \hat{\chi}_{2n} \cdot \mathbf{n} ds \cdot \hat{\theta}_2 \quad (11)$$

The left hand side is the first moment of the concentration field. The $\hat{\chi}_2$ operators vanish in volume integrands since, for a constant weighting function, $\nabla w = 0$. For snapshots with large enough V_n , we approximate the boundary term on the right as

$$\frac{1}{V_n} \Delta t \int_{\partial \Omega_n} \hat{\chi}_{2n} \cdot \mathbf{n} ds \cdot \hat{\theta}_2 \approx 0.$$

This assumes that the boundary integral of the flux is negligible when scaled by a length $\sim V_n/\text{vol}(\partial\Omega_n)$ given a sufficiently small time step, Δt . As a consequence, only algebraic (non-differential) operators remain:

$$\frac{1}{V_n} \int_{\Omega_n} C_n dv = \frac{1}{V_n} \Delta t \int_{\Omega_n} \chi_{1_n} dv \cdot \boldsymbol{\theta}_1 + \frac{1}{V_n} \int_{\Omega_n} C_{n-1} dv. \quad (12)$$

For Stage 2, we choose $w = C_n$ over Ω_n , to give:

$$\frac{1}{V_n} \int_{\Omega_n} C_n \frac{\partial C_n}{\partial t} dv = \frac{1}{V_n} \int_{\Omega_n} C_n \chi \cdot \boldsymbol{\theta} dv \quad (13)$$

$$\Rightarrow \frac{1}{V_n} \int_{\Omega_n} \frac{1}{2} \frac{\partial C_n^2}{\partial t} dv = \frac{1}{V_n} \int_{\Omega_n} C_n \chi \cdot \boldsymbol{\theta} dv \quad (14)$$

$$= \frac{1}{V_n} \int_{\Omega_n} C_n \chi_1 \cdot \boldsymbol{\theta}_1 dv + \frac{1}{V_n} \int_{\Omega_n} C_n \chi_2 \cdot \boldsymbol{\theta}_2 dv. \quad (15)$$

Again writing a backward difference approximation of the dynamics, using the divergence form as above and integrating by parts, we have:

$$\begin{aligned} \frac{1}{V_n} \int_{\Omega_n} C_n^2 dv &= \frac{1}{V_n} 2\Delta t \left(\int_{\Omega_n} C_n \chi_{1_n} dv \cdot \boldsymbol{\theta}_1 - \int_{\Omega_n} \nabla C_n \cdot \hat{\chi}_{2_n} dv \cdot \hat{\boldsymbol{\theta}}_2 \right) \\ &\quad + \frac{1}{V_n} 2\Delta t \int_{\partial\Omega_n} C_n \hat{\chi}_{2_n} \cdot \mathbf{n} ds \cdot \hat{\boldsymbol{\theta}}_2 + \frac{1}{V_n} \int_{\Omega_n} C_{n-1}^2 dv. \end{aligned} \quad (16)$$

The left hand side of Equation (16) is the second moment of the concentration field. Note that the boundary term is different than in Equation (11), and cannot be assumed to vanish even for large enough $V_n/\text{vol}(\partial\Omega_n)$. Before moving on with the formulation we emphasize that $\Omega_n \subseteq \Omega$ in Equations (12) and (16) can be the entire physical specimen, Ω , or any subdomain.

We now make the first of two assumptions guided by the experiments to which we seek to apply our methods. The volume-normalized first and second moments of C_n over a chosen subdomain can be approximated by the corresponding volume-normalized moments evaluated over different subdomains. This reflects the assumption, commonly made about the phenomena of interest in experiments, that the fields over each of these subdomains are statistically similar. Therefore, volume-normalization over subdomains corresponding to snapshots at different times results in approximate equality.

Assumption 1: Volume-normalized moments are approximately equal due to statistical similarity of the fields over different subdomains $\Omega_{i_n}, \Omega_{j_n}, \dots \subseteq \Omega$, $i, j = 1, 2, \dots$ at time t_n .

$$\frac{1}{V_{i_n}} \int_{\Omega_{i_n}} C_n^k dv \approx \frac{1}{V_{j_n}} \int_{\Omega_{j_n}} C_n^k dv, \quad \text{where } \Omega_{i_n}, \Omega_{j_n} \subseteq \Omega, \quad (17)$$

Assumption 1 allows us to use data collected over different subdomains, Ω_{i_n} , $i = 1, 2, \dots$ at time t_n . This further allows us to estimate the volume-normalized moments by replacing the integrals of C_{n-1} and C_{n-1}^2 over Ω_n in Equations (12) and (16), respectively by integrals of the same integrands, but over Ω_{n-1} :

$$\frac{1}{V_n} \int_{\Omega_n} C_n dv \approx \frac{1}{V_n} \Delta t \int_{\Omega_n} \chi_1 dv \cdot \boldsymbol{\theta}_1 + \frac{1}{V_{n-1}} \int_{\Omega_{n-1}} C_{n-1} dv \quad (18)$$

$$\begin{aligned} \frac{1}{V_n} \int_{\Omega_n} C_n^2 dv &\approx \frac{1}{V_n} 2\Delta t \left(\int_{\Omega_n} C_n \chi_1 dv \cdot \boldsymbol{\theta}_1 - \int_{\Omega_n} \nabla C_n \cdot \hat{\chi}_2 dv \cdot \hat{\boldsymbol{\theta}}_2 \right) + \frac{1}{V_{n-1}} \int_{\Omega_{n-1}} C_{n-1}^2 dv \\ &+ \frac{1}{V_n} 2\Delta t \int_{\partial\Omega_n} C_n \hat{\chi}_{2_n} \cdot \mathbf{n} ds \cdot \hat{\boldsymbol{\theta}}_2 \end{aligned} \quad (19)$$

Thus, the data C_k corresponding to a specific time instant, t_k need only be considered over the snapshot, Ω_k observed at that time in an experiment.

The second assumption is that the volume-normalized first and second moments of C_n over sub-domain Ω_n at time t_n can be approximated by the corresponding volume-normalized moments evaluated using data, \tilde{C}_n , collected from *different physical specimens* at time t_n . Here, the tilde denotes data from a different specimen. This reflects experimental practice in which data from different specimens are measured under the same conditions and physical time of the experiment, and statistical similarity is assumed. The mathematical and numerical equivalence to this procedure is modeled by employing the same initial condition with different spatially randomized perturbations. This is explained in detail in Section 2.5.1.

Assumption 2: Volume-normalized moments are approximated using data, \tilde{C}_n , from different physical specimens at the same time, t_n .

$$\frac{1}{V_n} \int_{\Omega_n} C_n^k dv \approx \frac{1}{\tilde{V}_n} \int_{\tilde{\Omega}_n} \tilde{C}_n^k dv \quad (20)$$

Assumptions 1 and 2 imply statistical similarity of fields over different subdomains and physical specimens at the same time. The data collected from pattern forming phenomena better satisfies the assumption of statistical similarity for larger subdomains because localized features are averaged out. The realization of statistical similarity in the data is discussed in Section 2.5.2. Replacing the

approximations by equalities in our VSI algorithm, Equations (18) and (19) can be rewritten as:

Stage 1:

$$\frac{1}{\Delta t} \left(\frac{1}{V_n} \int_{\Omega_n} C_n dv - \frac{1}{V_{n-1}} \int_{\Omega_{n-1}} C_{n-1} dv \right) = \frac{1}{V_n} \int_{\Omega_n} \chi_1 dv \cdot \theta_1 \quad (21)$$

Stage 2:

$$\begin{aligned} \frac{1}{2\Delta t} \left(\frac{1}{V_n} \int_{\Omega_n} C_n^2 dv - \frac{1}{V_{n-1}} \int_{\Omega_{n-1}} C_{n-1}^2 dv \right) - \frac{1}{V_n} \int_{\Omega_n} C_n \chi_1 dv \cdot \theta_1 &= -\frac{1}{V_n} \int_{\Omega_n} \nabla C_n \cdot \hat{\chi}_2 dv \cdot \hat{\theta}_2 \\ &+ \frac{1}{V_n} \int_{\partial\Omega_n} C_n \hat{\chi}_{2n} \cdot \mathbf{n} ds \cdot \hat{\theta}_2 \end{aligned} \quad (22)$$

Given data on C at suitable times, we define the left hand-sides of Equations (21) and (22) to be the labels. In Section 2.4 we show how they lead to target vectors in VSI, and the right-hand-sides lead to matrices of candidate basis operators.

We recall that, in the weak form, the choice of the weighting function $w^h \in \mathcal{V}^h$ is arbitrary. However, the judicious choice of w^h is critical for the success of VSI. A spatially constant w^h eliminates volume integrals of differential operators in the weak form leaving only algebraic (non-differential) operators as volume terms in Stage 1. The choice of $w^h = C^h$ in Stage 2 turns differential operators, such as the Laplace and biharmonic operators into quadratic forms in the weak form (see Section 2.3 below). This is suitable for pattern forming dynamics, because it ensures that the integrand of, e.g. $\int_{\Omega} \nabla C \cdot \nabla C dv$ is non-negative, and that the corresponding weak operators are identifiable. However certain choices of w^h could render some operators unidentifiable. For example, choosing $w^h = x_1$ (spatial coordinate), the integral $\int_{\Omega} \nabla x_1 \cdot \nabla C dv$ proves insignificant when evaluated over a (quasi-)periodic pattern. Contributions to this term are nearly cancelled out by the x_1 -symmetry of the (quasi-)periodicity that is seen, for instance, in Figure 1.

2.3 Candidate basis operators

Suppose we have data on certain degrees of freedom (DOFs) of a discretization, C^h , for a series of time steps. These DOFs are the nodal values in finite element methods, and the control variables if iso-geometric analytic methods are used. Using these DOFs, a Galerkin representation of the field could be constructed over the domain. Below we explain the procedure of generating candidate basis operators in weak form with three examples.

2.3.1 Weak forms of polynomial approximations of algebraic operators at time t_n with $w^h = 1$

$$\chi_{1_n}^{C^k,1} := \frac{1}{V_n} \int_{\Omega_n} (C_n^h)^k dv \quad (23)$$

The above equation represents all algebraic operators without loss of generality, since in principle they can all be expanded via polynomial expansions (e.g., Taylor series). If specific forms are desired, for instance exponential terms that are common in reaction terms, they would be used directly. While $w^h = C^h$ (and higher powers) does not eliminate algebraic operators in Stage 2, $w^h = 1$ does eliminate differential operators from the volume integrals allowing robust identification of the algebraic operators in Stage 1.

2.3.2 Weak form of the Laplacian operator at time t_n with $w^h = C^h$

Multiplying by the weighting function and integrating by parts, we have

$$\int_{\Omega_n} C_n^h \nabla^2 C_n^h dv = - \int_{\Omega_n} \nabla C_n^h \cdot \nabla C_n^h dv + \frac{1}{2} \int_{\partial\Omega_n} \nabla (C_n^h)^2 \cdot \mathbf{n} ds. \quad (24)$$

We define

$$\chi_{2_n}^{\nabla^2 C, C} = - \int_{\Omega_n} \nabla C_n \cdot \nabla C_n^h dv + \frac{1}{2} \int_{\partial\Omega_n} \nabla (C_n^h)^2 \cdot \mathbf{n} ds \quad (25)$$

as the Laplacian in weak form with $w^h = C^h$.

2.3.3 Weak form of the biharmonic operator $\nabla^4 C_n$ at time t_n with $w^h = C^h$

Multiplying by the weighting function and integrating by parts twice, we obtain

$$\int_{\Omega_n} w^h \nabla^4 C_n^h dv = \int_{\Omega_n} \nabla^2 C_n^h \nabla^2 C_n^h dv - \int_{\partial\Omega_n} \nabla C_n^h \cdot \mathbf{n} \nabla^2 C_n^h ds + \int_{\partial\Omega_n} C_n^h \nabla (\nabla^2 C_n^h) \cdot \mathbf{n} ds. \quad (26)$$

We then define

$$\chi_{2_n}^{\nabla^4 C, C} = \int_{\Omega_n} \nabla^2 C_n^h \nabla^2 C_n^h dv - \int_{\partial\Omega_n} \nabla C_n^h \cdot \mathbf{n} \nabla^2 C_n^h ds + \int_{\partial\Omega_n} C_n^h \nabla (\nabla^2 C_n^h) \cdot \mathbf{n} ds \quad (27)$$

as the biharmonic operator in weak form with $w^h = C^h$.

The second-order gradients in Equation (27) require the solutions and basis functions to lie in $\mathcal{H}^2(\Omega)$, while the Lagrange polynomial basis functions traditionally used in finite element analysis only lie in $\mathcal{H}^1(\Omega)$. We therefore draw the basis functions, ϕ^a in Equations (6) and (7), from the family of Non-Uniform Rational B-Splines (NURBS), and adopt Isogeometric Analysis (IGA) in our simulations to find the solutions in $\mathcal{H}^2(\Omega)$. A discussion of the NURBS basis and IGA is beyond the scope of this communication; interested readers are directed to the original works on this topic, such as Ref. [32] and references therein.

2.4 Identification of basis operators via two stage stepwise regression

To identify a dynamical system, we need to generate all possible basis operators, χ_1 and χ_2 , acting on the solution, compute the non-zero coefficient for each basis operator that is in the model (active bases), while also attaining coefficients of zero for the basis operators that are not in the model (inactive bases). We begin by putting together the right hand-sides of Equations (21) and (22) at each time $\{\dots, t_{n-1}, t_n, t_{n+1}, \dots\}$. Let

$$\mathbf{y}_1 = \begin{bmatrix} \vdots \\ \frac{1}{\Delta t} \left(\frac{1}{V_{n-1}} \int_{\Omega_{n-1}} C_{n-1} dv - \frac{1}{V_{n-2}} \int_{\Omega_{n-2}} C_{n-2} dv \right) \\ \frac{1}{\Delta t} \left(\frac{1}{V_n} \int_{\Omega_n} C_n dv - \frac{1}{V_{n-1}} \int_{\Omega_{n-1}} C_{n-1} dv \right) \\ \frac{1}{\Delta t} \left(\frac{1}{V_{n+1}} \int_{\Omega_{n+1}} C_{n+1} dv - \frac{1}{V_n} \int_{\Omega_n} C_n dv \right) \\ \vdots \end{bmatrix} \quad (28)$$

and

$$\mathbf{y}_2 = \begin{bmatrix} \vdots \\ \frac{1}{2\Delta t} \left(\frac{1}{V_{n-1}} \int_{\Omega_{n-1}} C_{n-1}^2 dv - \frac{1}{V_{n-2}} \int_{\Omega_{n-2}} C_{n-2}^2 dv \right) - \frac{1}{V_{n-1}} \int_{\Omega_{n-1}} C \chi_1 dv \cdot \boldsymbol{\theta}_1 \\ \frac{1}{2\Delta t} \left(\frac{1}{V_n} \int_{\Omega_n} C_n^2 dv - \frac{1}{V_{n-1}} \int_{\Omega_{n-1}} C_{n-1}^2 dv \right) - \frac{1}{V_n} \int_{\Omega_n} C \chi_1 dv \cdot \boldsymbol{\theta}_1 \\ \frac{1}{2\Delta t} \left(\frac{1}{V_{n+1}} \int_{\Omega_{n+1}} C_{n+1}^2 dv - \frac{1}{V_n} \int_{\Omega_n} C_n^2 dv \right) - \frac{1}{V_{n+1}} \int_{\Omega_{n+1}} C \chi_1 dv \cdot \boldsymbol{\theta}_1 \\ \vdots \end{bmatrix} \quad (29)$$

be the target vectors formed as labels from the data at the two stages, respectively. Likewise, we form the respective matrices, Ξ_1 and Ξ_2 , containing all possible operator bases:

$$\Xi_1 = \begin{bmatrix} \vdots & \vdots & \vdots & \vdots \\ \frac{1}{V_{n-1}} \int_{\Omega_{n-1}} 1 dv & \frac{1}{V_{n-1}} \int_{\Omega_{n-1}} C_{n-1} dv & \frac{1}{V_{n-1}} \int_{\Omega_{n-1}} C_{n-1}^2 dv & \dots \\ \frac{1}{V_n} \int_{\Omega_n} 1 dv & \frac{1}{V_n} \int_{\Omega_n} C_n dv & \frac{1}{V_n} \int_{\Omega_n} C_n^2 dv & \dots \\ \frac{1}{V_{n+1}} \int_{\Omega_{n+1}} 1 dv & \frac{1}{V_{n+1}} \int_{\Omega_{n+1}} C_{n+1} dv & \frac{1}{V_{n+1}} \int_{\Omega_{n+1}} C_{n+1}^2 dv & \dots \\ \vdots & \vdots & \vdots & \vdots \end{bmatrix} \quad (30)$$

$$\Xi_2 = \begin{bmatrix} \vdots & \vdots & \vdots \\ \chi_{2_{n-1}}^{\nabla^2 C, C} & \chi_{2_{n-1}}^{\nabla^4 C, C} & \dots \\ \chi_{2_n}^{\nabla^2 C, C} & \chi_{2_n}^{\nabla^4 C, C} & \dots \\ \chi_{2_{n+1}}^{\nabla^2 C, C} & \chi_{2_{n+1}}^{\nabla^4 C, C} & \dots \\ \vdots & \vdots & \vdots \end{bmatrix} \quad (31)$$

Then Equations (21) and (22) can be expressed as

$$\text{Stage 1:} \quad \mathbf{y}_1 = \Xi_1 \boldsymbol{\theta}_1 \quad (32)$$

and

$$\text{Stage 2: } \mathbf{y}_2(\boldsymbol{\theta}_1) = \boldsymbol{\Xi}_2 \boldsymbol{\theta}_2. \quad (33)$$

Equations (32) and (33) immediately deliver the two-stage algorithm of VSI, first for the coefficient vector $\boldsymbol{\theta}_1$, and then for $\boldsymbol{\theta}_2$ given the estimate of $\boldsymbol{\theta}_1$. Thus splitting the process into two stages also alleviates the curse of dimensionality as a smaller number of operators needs to be considered at each stage for parsimonious identification.

The coefficient vectors $\boldsymbol{\theta}_1$ and $\boldsymbol{\theta}_2$ in Equations (32) and (33) can be solved by minimizing the squared-norm loss functions l_1 and l_2 :

$$\boldsymbol{\theta}_1 = \arg \min_{\tilde{\boldsymbol{\theta}}_1} \left\{ l_1 := \left\| \mathbf{y}_1 - \boldsymbol{\Xi}_1 \tilde{\boldsymbol{\theta}}_1 \right\|_2^2 \right\} \quad (34)$$

$$\boldsymbol{\theta}_2 = \arg \min_{\tilde{\boldsymbol{\theta}}_2} \left\{ l_2 := \left\| \mathbf{y}_2 - \boldsymbol{\Xi}_2 \tilde{\boldsymbol{\theta}}_2 \right\|_2^2 \right\}, \quad (35)$$

which have analytical solutions expressible via the pseudo-inverses:

$$\boldsymbol{\theta}_1 = (\boldsymbol{\Xi}_1^T \boldsymbol{\Xi}_1)^{-1} \boldsymbol{\Xi}_1^T \mathbf{y}_1 \quad (36)$$

$$\boldsymbol{\theta}_2 = (\boldsymbol{\Xi}_2^T \boldsymbol{\Xi}_2)^{-1} \boldsymbol{\Xi}_2^T \mathbf{y}_2. \quad (37)$$

For robustness in the presence of noise and outliers, we use ridge regression to inject regularization. The optimization problems in Equations (34) and Equation (35) are then updated with additional penalty terms:

$$\boldsymbol{\theta}_1 = \arg \min_{\tilde{\boldsymbol{\theta}}_1} \left\{ l_1(\tilde{\boldsymbol{\theta}}_1) + \lambda_1 \left\| \tilde{\boldsymbol{\theta}}_1 \right\|_2^2 \right\} \quad (38)$$

$$\boldsymbol{\theta}_2 = \arg \min_{\tilde{\boldsymbol{\theta}}_2} \left\{ l_2(\tilde{\boldsymbol{\theta}}_2) + \lambda_2 \left\| \tilde{\boldsymbol{\theta}}_2 \right\|_2^2 \right\} \quad (39)$$

where λ_1 and λ_2 are regularization hyperparameters, with solutions

$$\boldsymbol{\theta}_1 = (\boldsymbol{\Xi}_1^T \boldsymbol{\Xi}_1 + \lambda_1 \mathbf{I})^{-1} \boldsymbol{\Xi}_1^T \mathbf{y}_1 \quad (40)$$

$$\boldsymbol{\theta}_2 = (\boldsymbol{\Xi}_2^T \boldsymbol{\Xi}_2 + \lambda_2 \mathbf{I})^{-1} \boldsymbol{\Xi}_2^T \mathbf{y}_2. \quad (41)$$

However, performing a standard, one-shot ridge regression for the full $\boldsymbol{\theta}$ vector will lead to a solution with nonzero contributions in all components of the vector. Such a solution of the system identification will be overfit to the data, (and potentially to noise in the data), and lose parsimony by failing to sharply delineate the relevant bases. Another option is to use compressive sensing

techniques [33, 34] that employ ℓ_1 -regularization, instead. However, we found their performance for system identification to be highly sensitive to the selection of regularization hyperparameters, leading to VSI results that are similar to one-shot ridge regression for $\boldsymbol{\theta}$. These observations then motivate us to take a different approach to iteratively eliminate the operators that have been identified to be inactive.

2.4.1 Stepwise regression

In this work, we use backward model selection by stepwise regression [35], which, as we have demonstrated, delivers parsimonious results with VSI [27]. The algorithm is summarized below.

Algorithm 1: Model selection by Stepwise regression:

Step 0: Establish target vector \mathbf{y} and matrix of bases Ξ .

Step 1: Solve $\boldsymbol{\theta}^i$ by the linear regression problems, Equations (32) and (33), using ridge regression. Calculate the loss function at this iteration, l^i .

Step 2: Eliminate basis operators in matrix Ξ by deleting their columns, using the F -test introduced below. Set to zero the corresponding components of $\boldsymbol{\theta}^i$.

GOTO Step 1. Note that at this stage the loss function remains small ($l^i \sim l^{i-1}$), and the solution may be overfit.

Step 3: The algorithm stops if the F -test does not allow elimination of any more basis operators. Beyond this, the loss function increases dramatically for any further reduction.

There are several choices for the criterion for eliminating basis terms. Here, we adopt a widely used statistical criterion called the F -test, also used by us previously [27]. The significance of the change between the model at iterations i and $i-1$ is evaluated by:

$$F = \frac{\frac{l^i - l^{i-1}}{p^{i-1} - p^i}}{\frac{l^{i-1}}{m - p^{i-1}}} \quad (42)$$

where p^i is the number of bases at iteration i and m is the total number of operator bases. Model selection is achieved through the following algorithm:

Algorithm 2: Model selection by the F -test:

Step 1:

Tentatively eliminate the basis corresponding to coefficients in θ^i which are smaller than the pre-defined threshold. Evaluate the F value followed by ridge regression on the reduced basis set.

Step 2:

IF $F < \alpha$

THEN formally eliminate these bases in matrix Ξ , by deleting the corresponding columns. GOTO Step 1.

ELSE GOTO Step 1, and choose another basis as a candidate for elimination.

In this work we adopt the threshold:

$$\text{threshold}^i = \hat{\theta}^i + \epsilon \quad (43)$$

$$\hat{\theta}^i = \arg \min_{\{\theta_\alpha^i\}_{\alpha=1}^m} |\theta_\alpha^i| \quad (44)$$

where, as defined in Equation (44) $\hat{\theta}^i$ is the component with the smallest magnitude in $\{\theta_\alpha^i\}_{\alpha=1}^m$, and ϵ is a small tolerance. The penalty coefficients in ridge regression, λ_1 and λ_2 , are chosen to lie in the range $[10^{-10}, 10^{-1}]$ by leave-one-out cross-validation at each iteration. The hyperparameter α is chosen to lie in the range $[1, 10]$, by five-fold cross validation. We summarize the stepwise regression algorithm and F -test in Figure 2.

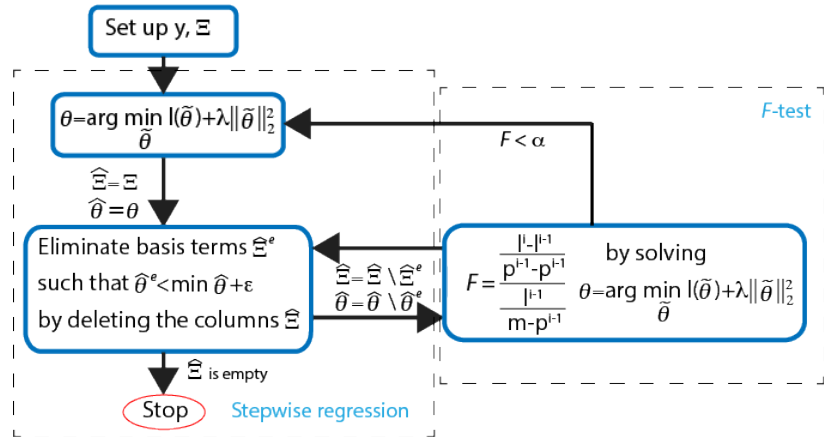


Figure 2: Schematic of the algorithms for stepwise regression and the F -test.

2.5 Variational System Identification with dynamic data

We now use the framework detailed in the preceding section to identify the parabolic PDEs that govern pattern formation. To test our methods, we deploy them here to identify PDEs using data synthesized through high-fidelity, direct numerical simulations (DNS) from known “true-solution” systems. We consider test cases with the following two pattern formation models for data generation, with their true parameter values summarized in Table 1:

Model 1:

$$\frac{\partial C_1}{\partial t} = D_1 \nabla^2 C_1 + R_{10} + R_{11}C_1 + R_{13}C_1^2 C_2 \quad (45)$$

$$\frac{\partial C_2}{\partial t} = D_2 \nabla^2 C_2 + R_{20} + R_{21}C_1^2 C_2 \quad (46)$$

$$\text{with } \nabla C_1 \cdot \mathbf{n} = 0; \quad \nabla C_2 \cdot \mathbf{n} = 0 \text{ on } \Gamma \quad (47)$$

where Γ is the domain boundary. Model 1 represents the coupled diffusion-reaction equations for two species following Schnakenberg kinetics [36], but with different boundary conditions. For an activator-inhibitor species pair, these equations use auto-inhibition with cross-activation of a short range species, and auto-activation with cross-inhibition of a long range species to form so-called Turing patterns [5].

Model 2:

$$\frac{\partial C_1}{\partial t} = \nabla \cdot (M_1 \nabla \mu_1) \quad (48)$$

$$\frac{\partial C_2}{\partial t} = \nabla \cdot (M_2 \nabla \mu_2) \quad (49)$$

$$\mu_1 = \frac{\partial g}{\partial C_1} - k_1 \nabla^2 C_1 \quad (50)$$

$$\mu_2 = \frac{\partial g}{\partial C_2} - k_2 \nabla^2 C_2 \quad (51)$$

$$\text{with } \nabla \mu_1 \cdot \mathbf{n} = 0; \quad \nabla C_1 \cdot \mathbf{n} = 0 \text{ on } \Gamma \quad (52)$$

$$\nabla \mu_2 \cdot \mathbf{n} = 0; \quad \nabla C_2 \cdot \mathbf{n} = 0 \text{ on } \Gamma \quad (53)$$

where g is a non-convex, “homogeneous” free energy density function, whose form has been chosen

from Ref. [14]:

$$g(C_1, C_2) = \frac{3d}{2s^4} \left((2C_1 - 1)^2 + (2C_2 - 1)^2 \right)^2 + \frac{d}{s^3} (2C_2 - 1) \left((2C_2 - 1)^2 - 3(2C_1 - 1)^2 \right) - \frac{3d}{2s^2} \left((2C_1 - 1)^2 + (2C_2 - 1)^2 \right). \quad (54)$$

Model 2 is a two-field Cahn-Hilliard system with fourth-order terms in the concentrations, C_1 and C_2 , which become apparent on substituting Equations (50) and (51) into (48) and (49), respectively. The three-well non-convex free energy density function (see Figure 3), $g(C_1, C_2)$, drives segregation of the system into two distinct phases. We have previously used this system to make connections with cell segregation in developmental biology [14]. The diffusion-reaction equations occur widely in

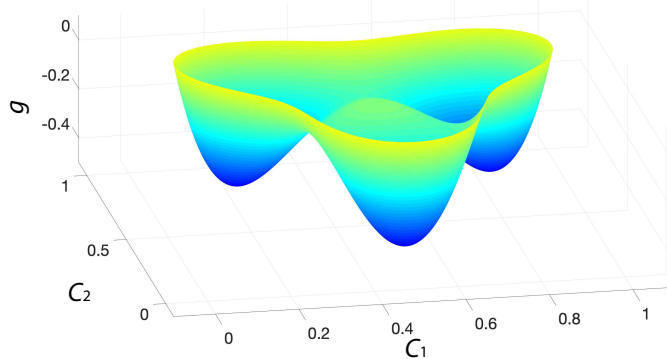


Figure 3: The three-well non-convex tissue energy density function.

the context of nucleation and growth phenomena in materials physics. The Cahn-Hilliard equation [4] also occupies a central role in the materials physics literature for modelling phase transformations developing from a uniform concentration field in the presence of a concentration instability.

D_1	D_2	R_{10}	R_{11}	R_{13}	R_{20}	R_{21}	M_1	M_2	k_1	k_2	d	s
1	40	0.1	-1	1	0.9	-1	0.1	0.1	10	10	0.4	0.7

Table 1: True parameter values used in DNS for synthesizing test data.

Substituting the parameter values from Table 1, we present the weak form of each model:

Model 1:

$$\int_{\Omega} w_1 \frac{\partial C_1}{\partial t} dv = \int_{\Omega} -1 \nabla w_1 \cdot \nabla C_1 dv + \int_{\Omega} w_1 (0.1 - C_1 + 1C_1^2 C_2) dv \quad (55)$$

$$\int_{\Omega} w_2 \frac{\partial C_2}{\partial t} dv = \int_{\Omega} -40 \nabla w_2 \cdot \nabla C_2 dv + \int_{\Omega} w_2 (0.9 - 1C_1^2 C_2) dv \quad (56)$$

Model 2:

$$\begin{aligned}
\int_{\Omega} w_1 \frac{\partial C_1}{\partial t} dv &= \int_{\Omega} \nabla w_1 \cdot (-17.8126 + 47.98C_1 + 21.591C_2 - 47.98C_1^2 - 15.9933C_2^2) \nabla C_1 dv \\
&+ \int_{\Omega} \nabla w_1 \cdot (-10.7955 + 21.591C_1 + 15.9933C_2 - 31.9867C_1C_2) \nabla C_2 dv \\
&+ \int_{\Omega} -1 \nabla^2 w_1 \nabla^2 C_1 dv
\end{aligned} \tag{57}$$

$$\begin{aligned}
\int_{\Omega} w_2 \frac{\partial C_2}{\partial t} dv &= \int_{\Omega} \nabla w_2 \cdot (-10.7955 + 21.591C_1 + 15.9933C_2 - 31.9867C_1C_2) \nabla C_1 dv \\
&+ \int_{\Omega} \nabla w_2 \cdot (-12.2149 + 15.9933C_1 + 42.3823C_2 - 15.9933C_1^2 - 47.98C_2^2) \nabla C_2 dv \\
&+ \int_{\Omega} -1 \nabla^2 w_2 \nabla^2 C_2 dv
\end{aligned} \tag{58}$$

2.5.1 Data preparation

All computations have been implemented in the `mechanoChemIGA` code framework, a library for modeling mechano-chemical problems using isogeometric analytics, available at <https://github.com/mechanoChem/mechanoChem>. The IBVPs presented here are two-dimensional. The initial conditions for all simulations are a constant value corrupted with random noise at each grid point:

$$C_{1,i} = 0.5 + \delta_{1,i} \tag{59}$$

$$C_{2,i} = 0.5 + \delta_{2,i} \tag{60}$$

where $\delta_{1,i}, \delta_{2,i} \sim \mathcal{U}(-0.01, 0.01)$ are independent (across i), uniform, random variables at each nodal mesh point i .

To mimic the experimental data that would be necessarily collected from multiple physical specimens due to the destructive nature of the acquisition procedure, we run each model for 30 different simulations, each with an independently and identically distributed realization of the initial condition in Equations (59) and (60) (e.g., see upper plots in Figure 4). The patterns generated from separate simulations, with initial conditions randomized as above, are non-identical but statistically similar (e.g., see lower plots in Figure 4). In this study we collected the data at 30 time steps, each over a spatially unrelated snapshot from a different simulation. Therefore, the total dataset of 30 snapshots does not correspond to a common initial condition or spatial subdomain.

The experimental data may also be noisy and of varying sparsity, often available only at low spatial resolution due to cost limitations or accessibility constraints of historical data. To mimic

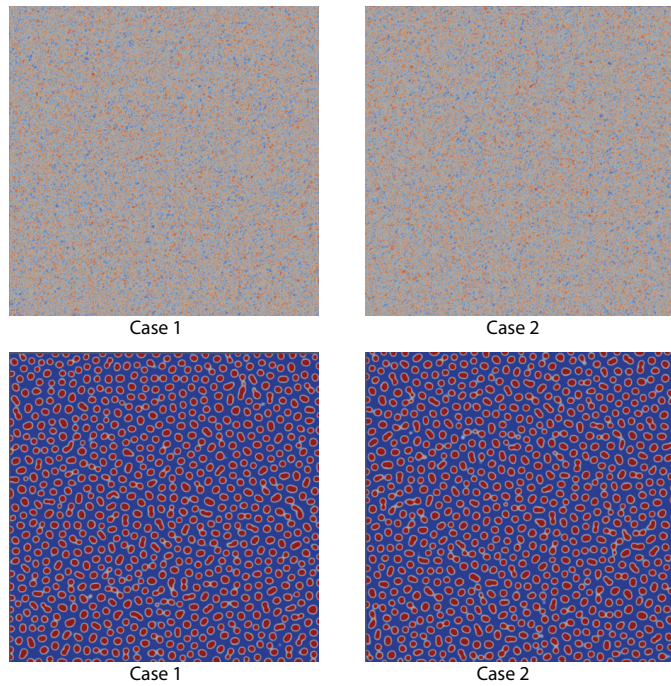


Figure 4: Upper plots: Concentration at $t = 0$ of two cases representing distinct experimental specimens. The perturbation is re-generated for every simulation. Lower plots: Concentration at $t = 20$. The Turing patterns generated from different initial conditions are statistically similar.

noisy data, we superpose the synthetic solutions C_1 and C_2 with an independent Gaussian noise $\mathcal{N}(0, \sigma^2)$ at each grid point. To simulate scenarios with different data sparsity, we use the full 400×400 domain as well as proportionally smaller subdomains of 300×300 , 200×200 , 100×100 and 50×50 meshes. These proper subsets represent incomplete data and, as discussed, could possibly come from spatially unrelated and even non-overlapping subdomains at different times. Having clean and noisy snapshots at varying sparsity, from different simulations representing distinct specimens and unrelated, non-overlapping subdomains, we generate 34 candidate basis operators in addition to the time derivative terms, summarized in Table 2.

Table 2: Candidate basis operators for model selection. Asterisks, (*) in the left column represent algebraic operators on C_1 and C_2 .

Type of basis	Basis in weak form			
$\nabla(*\nabla C_1)$	$\int_{\Omega} \nabla w \nabla C_1 dv$	$\int_{\Omega} \nabla w C_1 \nabla C_1 dv$	$\int_{\Omega} \nabla w \nabla C_2 dv$	
	$\int_{\Omega} \nabla w C_1^2 \nabla C_1 dv$	$\int_{\Omega} \nabla w C_1 C_2 \nabla C_1 dv$	$\int_{\Omega} \nabla w C_2^2 \nabla C_1 dv$	
	$\int_{\Omega} \nabla w C_1^3 \nabla C_1 dv$	$\int_{\Omega} \nabla w C_1^2 C_2 \nabla C_1 dv$	$\int_{\Omega} \nabla w C_1 C_2^2 \nabla C_1 dv$	$\int_{\Omega} \nabla w C_2^3 \nabla C_1 dv$
$\nabla(*\nabla C_2)$	$\int_{\Omega} \nabla w \nabla C_2 dv$	$\int_{\Omega} \nabla w C_1 \nabla C_2 dv$	$\int_{\Omega} \nabla w \nabla C_2 dv$	
	$\int_{\Omega} \nabla w C_1^2 \nabla C_2 dv$	$\int_{\Omega} \nabla w C_1 C_2 \nabla C_2 dv$	$\int_{\Omega} \nabla w C_2^2 \nabla C_2 dv$	
	$\int_{\Omega} \nabla w C_1^3 \nabla C_2 dv$	$\int_{\Omega} \nabla w C_1^2 C_2 \nabla C_2 dv$	$\int_{\Omega} \nabla w C_1 C_2^2 \nabla C_2 dv$	$\int_{\Omega} \nabla w C_2^3 \nabla C_2 dv$
$\nabla^2(*\nabla^2 C)$	$\int_{\Omega} \nabla^2 w \nabla^2 C_1 dv$	$\int_{\Omega} \nabla^2 w C_1 \nabla^2 C_1 dv$	$\int_{\Omega} \nabla^2 w \nabla^2 C_2 dv$	$\int_{\Omega} \nabla^2 w C_2 \nabla^2 C_2 dv$
non-gradient	$-\int_{\Omega} w 1 dv$	$-\int_{\Omega} w C_1 dv$	$-\int_{\Omega} w C_2 dv$	
	$-\int_{\Omega} w C_1^2 dv$	$-\int_{\Omega} w C_1 C_2 dv$	$-\int_{\Omega} w C_2^2 dv$	
	$-\int_{\Omega} w C_1^3 dv$	$-\int_{\Omega} w C_1^2 C_2 dv$	$-\int_{\Omega} w C_1 C_2^2 dv$	$-\int_{\Omega} w C_2^3 dv$

2.5.2 Statistical similarity in the data of pattern forming physics

Statistical similarity in the data is due to the random distribution of features/particles in the patterns. Before identifying the governing equations, we examine the validity of Assumptions 1 and 2 made in Section 2.2 using the steady state data generated by Model 1. The patterns formed by the diffusion-reaction system reach steady state as shown in Figure 5. The “particles” representing high concentrations of one species, attain random distribution over the entire domain, with average spacing, $d \approx 5$. Figures 6 and 7 show the first and second moments of C_1 and C_2 evaluated using data with different sizes of snapshots from separate simulations. The random perturbation affects the local features of C_1 and C_2 ; however, with increasing size of snapshots the statistical similarity becomes evident. Consequently moments evaluated using data from snapshots converge to the moments using full field data on the entire domain, thus validating Assumption 1. Moments evaluated using data from all 30 different simulations converge together, thus validating Assumption 2. The statistics start to converge when snapshots are bigger than 50×50 , and show

very low variance relative to the entire domain when snapshots exceed 200×200 . In other words, statistical similarity become more evident as the ratio of particle spacing to the snapshots' linear dimension decreases (0.1 for 50×50 snapshot and 0.025 for 200×200 snapshot).

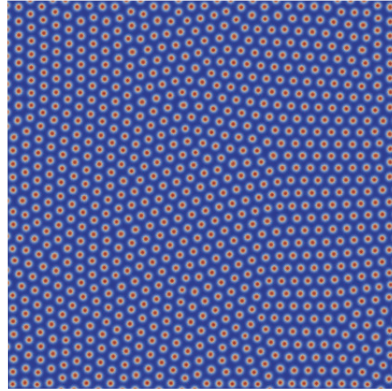


Figure 5: The C_1 concentration field generated by Model 1 at steady state.

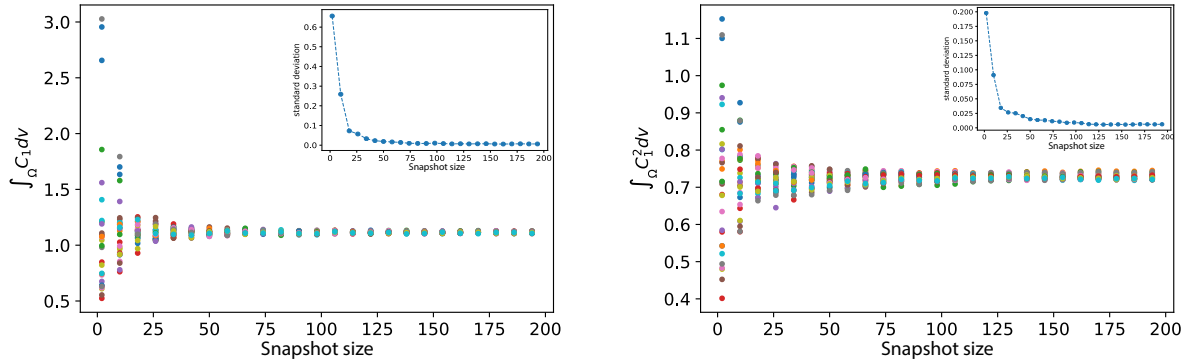


Figure 6: The first (left plot) and second moment (right plot) of C_1 evaluated using data generated by Model 1 from 30 simulations, marked by different colors, with different randomized initial conditions modeling data from different specimens. The embedded subplot shows the decreasing standard deviation of moments, evaluated using data from these 30 simulations (specimens). In the main and sub-plot, note the convergence with increasing snapshot size.

2.6 Numerical examples

The approximation of time derivatives needs data from at least two time steps, which are collected from different subdomains of the same simulation, or from simulations with different initial conditions, as discussed above. Our first example uses noise-free data. Figure 8 shows the time derivatives constructed using data collected from different sizes of snapshots at each time step.

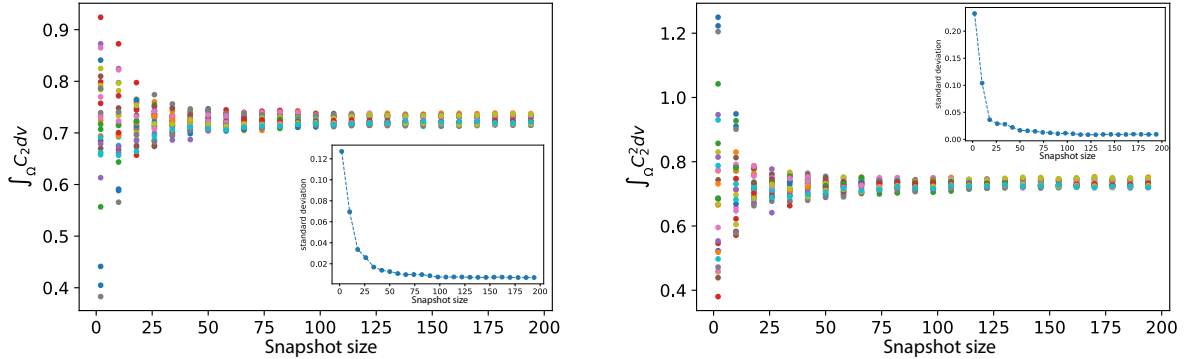


Figure 7: The first (left plot) and second moment (right plot) of C_2 evaluated using data generated by Model 1 from 30 simulations with different randomized initial conditions, marked by different colors. The different randomized initial conditions model data from different specimens. The embedded subplot shows the decreasing standard deviation of moments, evaluated using data from these 30 simulations (samples). In the main and sub-plot, note the convergence with increasing snapshot size.

Smaller snapshots yield high variance resulting from the initial condition's randomness (since we are utilizing noise-free data presently), especially at later times. This is because variations with time are small when the dynamical system is close to steady state, and are easily dominated by the variance induced by initial conditions. Their poor representation sabotages system identification, as we will discuss below.

We successfully identified the algebraic operators in the governing equation for C_1 in Stage 1, as shown in Figure 9. The stem and leaf plots (left panel) show the coefficient of each operator scaled by its true value. The loss remains small until it converges (right panel). VSI using data collected from larger snapshots yields lower losses, which also increase more dramatically compared to results using smaller snapshots, when an active operator is eliminated by trial in the stepwise regression process. In Stage 2 we successfully identified the one gradient dependent operator in the governing equation shown in Figure 10. We notice that in Stage 1 the gradually increasing loss function using data collected from small snapshots (50×50 mesh) allows a relatively small threshold in the F -test ($\alpha \sim 1$) to distinguish active and inactive operators. On the other hand, in Stage 2 the loss functions increase by half an order of magnitude in the last few iterations for the 100×100 and 50×50 cases, thus needing a higher F -test threshold ($\alpha \sim 10$) to distinguish inactive operators. These changes in loss function trajectories present a challenge in selecting α for the F -test, which must be achieved via cross validation to balance model complexity and accuracy.

Figure 11 shows that the algebraic operators in the governing equation for C_2 are correctly

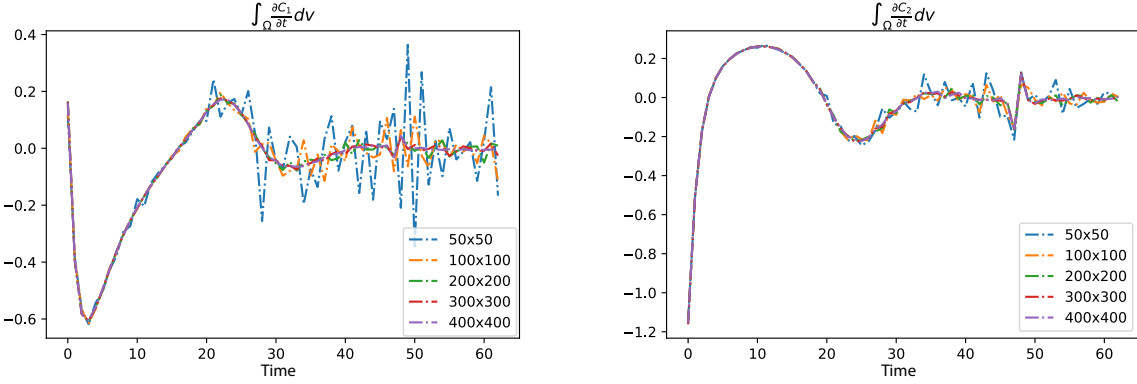


Figure 8: Time evolution of $\int_{\Omega} \frac{\partial C_1}{\partial t} dv$ and $\int_{\Omega} \frac{\partial C_2}{\partial t} dv$. Time derivatives constructed from small snapshots show higher variance due to initial conditions close to steady state.

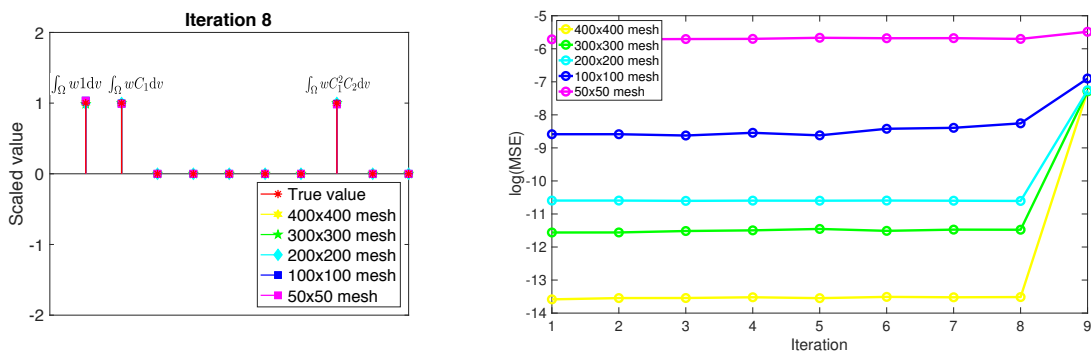


Figure 9: Inferred operators for C_1 from Stage 1 (left panel), and the loss (right panel) at each iteration using data generated from Model 1. The identified coefficients of active operators are scaled by their true values. The algorithm converges at iteration 8, beyond which the loss increases dramatically if any more operators are eliminated.

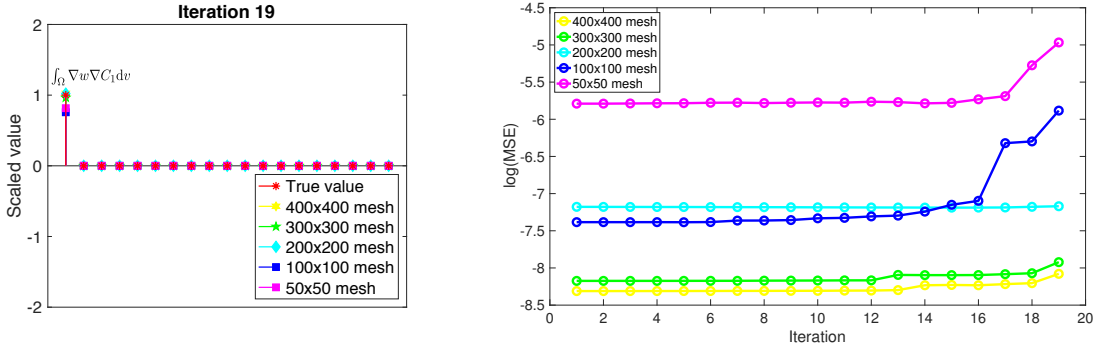


Figure 10: Inferred operators for C_1 from Stage 2 (left panel), and the loss (right panel) at each iteration using data generated from Model 1. The identified coefficients of active operators are scaled by their true values. The algorithm converges at iteration 19 with only one operator remaining.

identified. The loss functions remain small while a number of inactive operators are eliminated, and increase dramatically if any of the remaining active operators are eliminated beyond iteration 9. This is because the time derivative term (right plot in Figure 8) is well approximated even using data collected from small snapshots. In Stage 2, using the 50×50 dataset, the loss remains low while operators are eliminated by the F -test, but the sparsity of data leads to the active Laplacian operator being wrongly eliminated at an early iteration, as shown in Figure 12. With the 100×100 dataset, the Laplacian operator is also wrongly eliminated at the penultimate iteration. Note that the only surviving operators with these smaller snapshots are different than that identified with the larger snapshot datasets. With the 200×200 and **(zh)** larger snapshots, the Laplacian operator is correctly identified as the sole active operator and the stepwise regression algorithm terminates after 14 iterations. The full set of VSI results using noise-free data generated from Model 1 are also summarized in Table 5.

Next, we superimpose noise with zero mean and standard deviation $\sigma = 0.01$ over the data generated from Model 1. The noise on C_1 and C_2 gets amplified in the time derivative and spatial gradients. As shown in Figure 13, the noise dominates the true value of the Laplacian $\nabla^2 C_1$. The amplification of noise in the differential operators can cause failure of VSI that works with full-field data, as shown by Wang et al. [27]. However due to the integral nature of the first and second moments in the two stage VSI presented in this work, the noise is smoothed out. The zero mean ensures that the operators constructed with specific weighting functions are insensitive to noise. The algebraic operators are indeed successfully identified at Stage 1 using noisy data, as shown in Figure 14, and the single active differential operator, the Laplacian, is also identified in Stage 2 as shown in Figure 15. However, the loss function is in general higher than with noise-free data, and the error in the coefficients of the identified operators is also higher. For the governing equation of C_2 , all algebraic operators are successfully identified at Stage 1 using noisy data as shown in

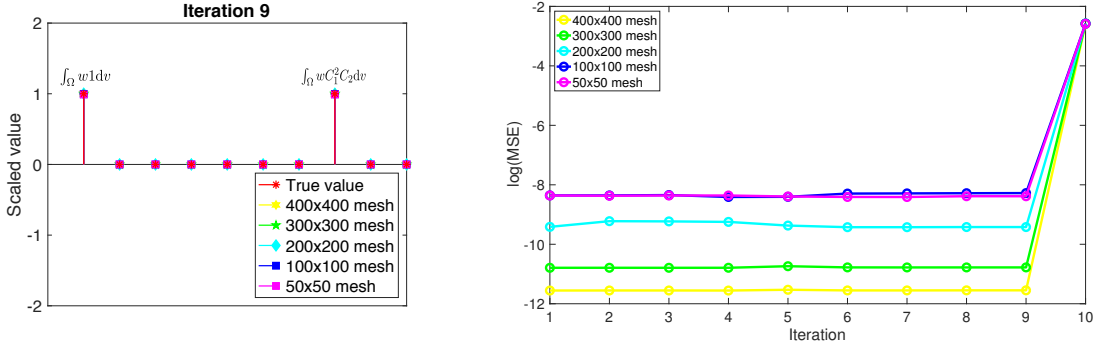


Figure 11: Inferred operators for C_2 from Stage 1 (left panel), and the loss (right panel) at each iteration using data generated from Model 1. The identified coefficients of active operators are scaled by their true values. The algorithm converges at iteration 9, beyond which the loss increases dramatically if any more operators are eliminated.

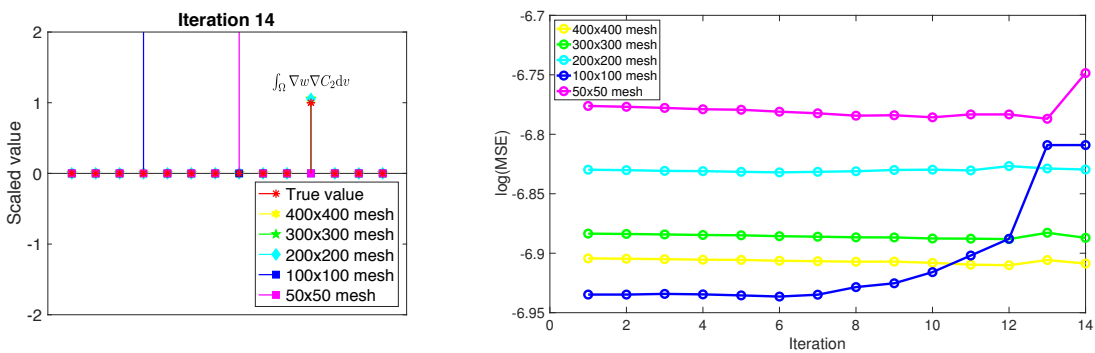


Figure 12: Inferred operators for C_2 from Stage 2 (left panel), and the loss (right panel) at each iteration using data generated from Model 1. The identified coefficients of active operators are scaled by their true values. The algorithm converges at iteration 14 with only one operator remaining. Note that the 200×200 and larger snapshots correctly identify the Laplacian, which is, however, incorrectly eliminated by the 50×50 and 100×100 snapshots.

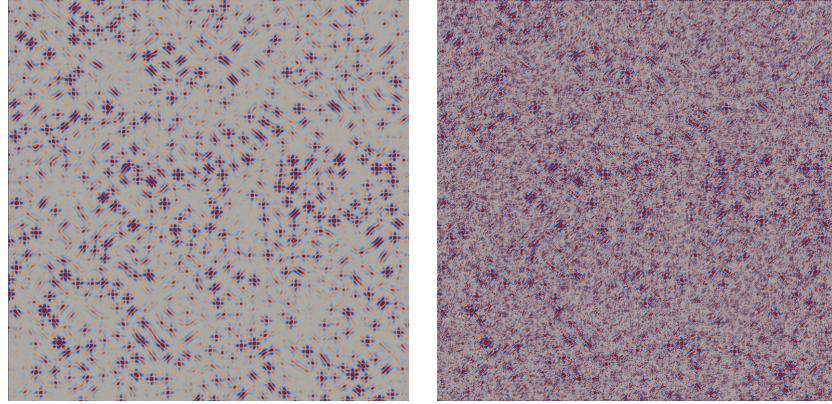


Figure 13: Noise-free (left) and noisy (right) fields of $\nabla^2 C_1$.

Figure 16. The single active differential operator, the Laplacian, is wrongly identified using smaller snapshots (200×200 , 100×100 and 50×50 datasets), as shown in Figure 17, while the larger snapshots allow its correct identification. The full set of VSI results using noisy data generated from Model 1 are summarized in Table 6.

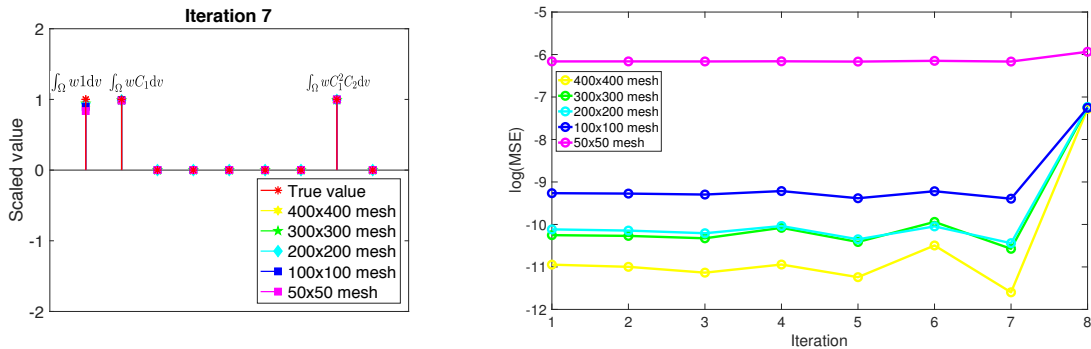


Figure 14: Inferred operators for C_1 at Stage 1 (left panel), and the loss (right panel) at each iteration using noise ($\sigma = 0.01$) superimposed on data generated from Model 1. The identified coefficients of active operators are scaled by their true values. The algorithm converges at iteration 7, beyond which the loss increases dramatically if any more active operators are eliminated.

Unlike the diffusion-reaction system, Model 2, represented by Cahn-Hilliard equations, is conservative. Consequently the time derivative of the first moment vanishes: $\frac{d}{dt} \int_{\Omega} C_n dv = 0$. The second moment, as well as other weak forms of algebraic and differential operators with $w^h = 1$ and $w^h = C^h$ also evolve very slowly after the initial regime of spinodal decomposition. With limited dynamic data, identifying the Cahn-Hilliard equations is challenging using the two stage VSI. However, we next present an alternate approach that leverages the data at steady state to successfully identify both diffusion-reaction and Cahn-Hilliard systems.

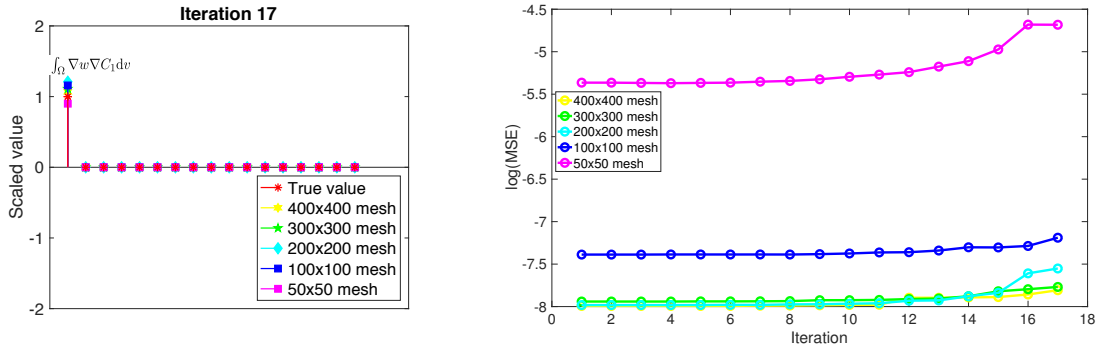


Figure 15: Inferred operators for C_1 at Stage 2 (left panel), and the loss (right panel) at each iteration using noise ($\sigma = 0.01$) superimposed on data generated from Model 1. The identified coefficients of active operators are scaled by their true values. The algorithm converges at iteration 17 with a single active operator remaining.

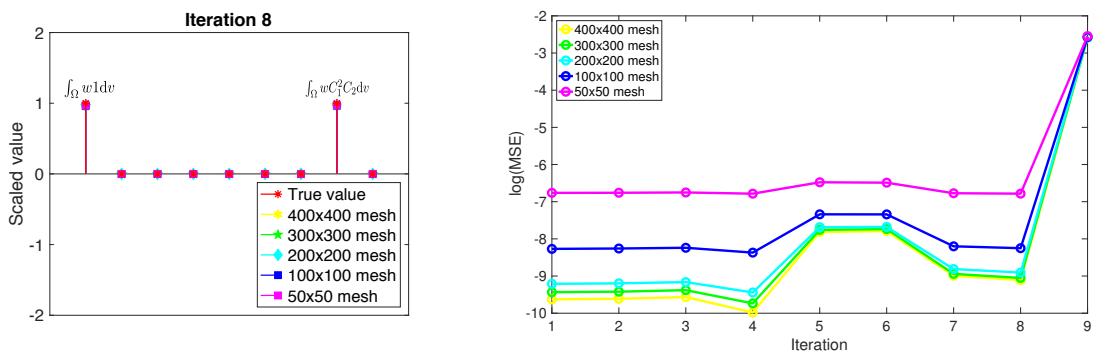


Figure 16: Inferred operators for C_2 at Stage 1 (left panel), and the loss (right panel) at each iteration using noise ($\sigma = 0.01$) superimposed on data generated from Model 1. The identified coefficients of active operators are scaled by their true values. The algorithm converges at iteration 8, beyond which the loss increases dramatically if any more active operators are eliminated.

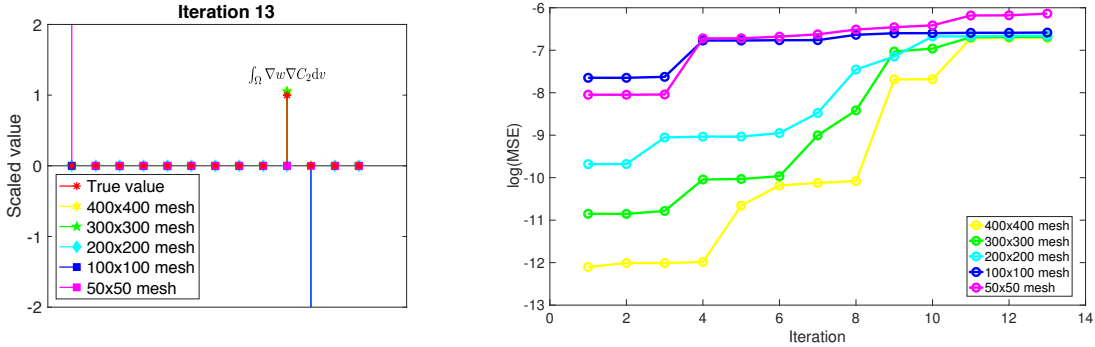


Figure 17: Inferred operators for C_2 at Stage 2 (left panel), and the loss (right panel) at each iteration using noise ($\sigma = 0.01$) superimposed on data generated from Model 1. The identified coefficients of active operators are scaled by their true values. The algorithm converges at iteration 14 with a single active operator remaining. The 300×300 and 400×400 snapshots correctly identify the Laplacian, but the smaller snapshots fail to do so.

3 Variational System Identification with dynamic and steady state data

One challenge of the two-stage procedure introduced in Section 2 is data availability, where experimental measurements from the dynamic regime (non-steady state) of the system can be especially difficult and expensive to obtain. While the regression problems in Equations (32) and (33) generally require over-determined systems to arrive at good solutions, this consequently demands a large dataset to delineate the relevant bases, since the number of rows in Equations (32) and (33) is the number of time instants minus one. The challenge posed by spatially unrelated data and sparse time instants led us to the two-stage formulation of the problem with integral forms as presented above in Section 2.2. This treatment, however, sacrifices any high spatial resolution available in the experimental snapshots. As a remedy, we have developed an approach that leverages data with high spatial resolution at steady state (or near-steady state). With this new approach, it is possible to first identify all operators up to a scaling factor, which is determined by the dynamics. Inference of this scaling factor, controlled by the dynamics, can then be achieved using only one of the two stages described previously for the algebraic and differential operators. The essence of the VSI approach, namely, the treatment of equations in weak form, remains unchanged.

3.1 Variational System Identification of basis operators with steady state data

Data with high spatial resolution at steady state, or near-steady state, is typically obtained from modern microscopy methods. In fact the data satisfying the steady state equation:

$$\chi \cdot \boldsymbol{\theta} = 0, \quad (61)$$

already provide rich information about the spatial operators (that is, other than time derivatives) in the system. By choosing a nontrivial χ_1 to be the target operator, the equation can be rewritten as:

$$-\chi_1 = \frac{1}{\theta_1} \bar{\chi} \cdot \bar{\boldsymbol{\theta}}, \quad (62)$$

where $\bar{\chi} = \chi \setminus \{\chi_1\}$ and $\bar{\boldsymbol{\theta}} = \boldsymbol{\theta} \setminus \{\theta_1\}$. We are able to identify the coefficients, $\bar{\boldsymbol{\theta}}$, up to a scaling constant, θ_1 , using the data at steady state by VSI [27]. However, in the absence of prior knowledge about the system, it may be the case that the selected target operator, χ_1 , is actually inactive (i.e., its prefactor $\theta_1 = 0$). Then Equation (62) is not valid for the data. Under such conditions, VSI will fail at parsimonious representation over the operators included in $\bar{\chi}$. “False” outcomes can then be detected by inconsistencies in the system identification, as we elaborate via examples below. On the other hand, if in two (or more) trials distinct operators are chosen as targets, and if these chosen targets are all indeed active in the true system, then the same set $\bar{\chi}$ will be identified in these different trials with coefficients $\bar{\boldsymbol{\theta}}$ differing only by a scaling factor. This consistency, up to a scaling factor, provides a confirmation test for VSI of the spatial operators with (near-)steady state data without the need for prior knowledge.

However, when confronted with data on systems that are governed by multiple equations, the above approach to identify consistent sets of active operators via the confirmation test can break down. In particular, this can happen if one of the equations has only one operator that is distinct from those appearing in other equations governing the system, and its remaining operators number fewer than in any other equation of the system. In such a situation, the stepwise regression algorithm will detect the steady state equation with the greater number of operators as the only consistent set passing the confirmation test. Even the choice of the one distinct operator in the remaining equation as target operator will not pass the confirmation test for consistency (since upon looking for consistency, the equation with greater number of operators will be identified as it provides a feasible solution with lower loss). Our approach to this detection of only the lower loss solution is to deliberately suppress an operator in a consistent set that passes the confirmation test. This forces the stepwise regression algorithm to detect the equation with fewer operators, provided the suppressed operator is indeed inactive in this set. Subsequent consistency checks with the correctly suppressed operator will pass the confirmation test. The combined confirmation test for consistency with operator suppression appears as Algorithm 3.

Algorithm 3: Confirmation Test of Consistency with Operator Suppression:

Let $N_\chi := \#\chi$ (where $\#$ denotes cardinality) and $N_{\text{field}} :=$ number of unknown fields in data (e.g., for data on C_1, C_2 , $N_{\text{field}} = 2$)

Function: Test of Consistency

```

FOR  $i = 1, \dots, N_\chi$ 
    With  $\chi_i$  as target vector, do stepwise regression to identify coefficients
     $\vartheta_i \in \mathbb{R}^{N_\chi-1}$ .
    IF  $i \geq 2$  &&  $\vartheta_i = \alpha \vartheta_j$  for  $j < i$  THEN
        Confirmation Test:  $\vartheta_i$  and  $\vartheta_j$  represent the same consistent set
    ELSE
         $\vartheta_i$  is inconsistent
    Collect all linearly independent consistent coefficient sets expressible as
     $\theta_\alpha \vartheta_\alpha, \theta_\beta \vartheta_\beta, \dots$  for  $\alpha, \beta, \dots \in \{1, \dots, N_\chi\}$ .

    While (True):
        Call Test of Consistency.
        IF  $\#\{\alpha, \beta, \dots\} < N_{\text{field}}$ 
            FOR  $i \in \{\alpha, \beta, \dots\}$ 
                Define  $\hat{\chi}_k$  to be the operator with coefficient  $\theta_{i_k}$  in  $\vartheta_i = \{\dots, \theta_{i_k}, \dots\}$ .
            Call Test of Consistency with  $\chi \setminus \hat{\chi}_k$ .
        ELSE
            EXIT

```

Thereafter, there remains only one unknown in the governing equations, which is the scaling factor, θ_1 :

$$\frac{\partial C}{\partial t} - \theta_1(\chi \cdot \theta) = 0, \quad (63)$$

which then can be identified using dynamic data and one of the two stages of VSI detailed in Sections 2.2–2.4. If an algebraic/differential operator was identified via Algorithm 3 for the (near-) steady state data, Stage 1/Stage 2 can be used respectively (Section 2.2). This is elaborated with examples in Section 3.2, and proves to be a powerful feature in favor of robustness and consistency of VSI for steady and dynamic data.

3.2 Numerical examples of with steady state and dynamic data

The steady state form of Model 1 in strong form is:

$$D_1 \nabla^2 C_1 + R_{10} + R_{11}C_1 + R_{13}C_1^2 C_2 = 0 \quad (64)$$

$$D_2 \nabla^2 C_2 + R_{20} + R_{21}C_1^2 C_2 = 0 \quad (65)$$

Given steady state, or near-steady state data, such as for full field or snapshots of diffusion-reaction systems in Figure 5, VSI can identify the steady state governing equations using the Confirmation Test of Consistency with Operator Suppression in Algorithm 3. As discussed in Section 3.1, choosing inactive operators to be targets yields inconsistent results. As shown in Figure 18, choosing two different (inactive) operators, $\int_{\Omega} \nabla w \cdot C_1 \nabla C_1 dv$ and $\int_{\Omega} \nabla w \cdot C_2 \nabla C_1 dv$ (in weak form), as targets, the identified results are completely different. The set of identified operators with $\int_{\Omega} \nabla w \cdot C_1 \nabla C_1 dv$ as target contains $\int_{\Omega} \nabla w \cdot C_2 \nabla C_1 dv$ but not *vice versa*. This is because choosing an inactive operator as the target removes it from the stepwise regression and model selection procedures in Algorithms 1 and 2, meaning that it has to be included in the identified set. Consequently, the identified sets of operators do not form a group of governing PDEs that models meaningful physics. This is reflected in the inconsistency between the operator sets.

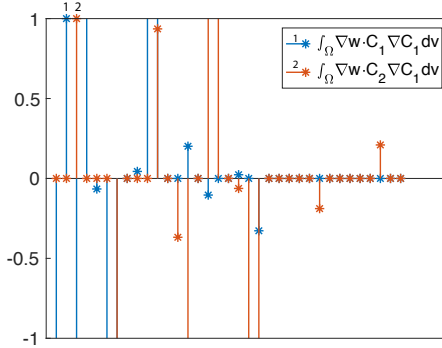


Figure 18: One example of inconsistently inferred operators with different targets using data at steady state. Choosing $\int_{\Omega} \nabla w \cdot C_1 \nabla C_1 dv$, labelled by 1, as target operator leads to a set of operators being identified, shown by the blue stems and leaves. This includes the operator $\int_{\Omega} \nabla w \cdot C_2 \nabla C_1 dv$ labelled by 2. However, choosing the latter as the target operator yields a different active set, shown as the orange stems and leaves. Both target operators are actually inactive, leading to inconsistency between the respective sets.

On the other hand, choosing the active operators as the targets does yield consistent identification. The plot on the left in Figure 19 shows that the identified set is consistent up to a scaling factor, with four different operators as, shown in the legend, as targets. This set identifies

the steady state equation (64). Note that the weak form operators $\int_{\Omega} w dv$ and $\int_{\Omega} w C_2 C_2^2 dv$ are common to Equations (64) and (65), but choosing either as target only yields the consistent set in Equation (64); i.e., the one with more operators, because this set leads to a lower loss. Suppression of either of the identified active operators $\int_{\Omega} \nabla w \cdot \nabla C_1 dv$ or $\int_{\Omega} w C_1 dv$, yields another set of consistent inferred operators, shown in the legend on the right in Figure 19. This set identifies the steady state equation for C_2 . This is a manifestation of the Confirmation Test of Consistency with Operator Suppression in Algorithm 3.

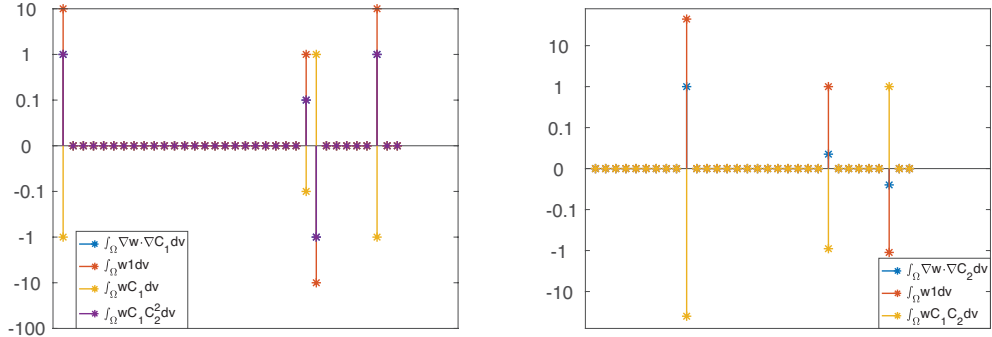


Figure 19: Two sets (left and right) of consistently inferred operators with different targets using data generated from Model 1 at steady state. The coefficient values have been plotted on the logarithmic scale in order to make them discernible across orders of magnitude. Each set consists of the operators in the legend of the corresponding sub-plot and is consistent up to a scaling factor. Note that the second set of consistently inferred operators is obtained on a reduced library of candidate operators without $\int_{\Omega} \nabla w \cdot \nabla C_1 dv$ or $\int_{\Omega} w C_1 dv$, the two operators in the first set of consistent inferred operators. The two sets, left and right, are the steady state equations for C_1 and C_2 in Equations (64) and (65), respectively.

In the following we choose the two Laplacian operators, $\nabla^2 C_1$ and $\nabla^2 C_2$, as targets and infer the remaining operators, $\bar{\chi}$:

$$\nabla^2 C_1 = \frac{1}{\theta_{D_1}} \bar{\chi} \cdot \bar{\theta} \quad (66)$$

$$\nabla^2 C_2 = \frac{1}{\theta_{D_2}} \bar{\chi} \cdot \bar{\theta}. \quad (67)$$

Without noise, very accurate results are obtained as shown in Figures 20 and 21 even with small snapshots. Next, using Stage 2 of the VSI approach, i.e. by choosing the weighting function to be $w^h = C_1^h$ and $w^h = C_2^h$, the diffusion coefficients θ_{D_1} and θ_{D_2} in Equations (66) and (67) are correctly identified as shown in Table 3. Recall that the diffusion coefficients are not identifiable from early time data collected with small snapshots as discussed before (See Figure 12, where

this failure was cast in terms of the Laplacian operator). However, they are identified using the Confirmation Test of Consistency with Operator Suppression (Algorithm 3) in combination with Stage 2 of the VSI approach (Algorithms 1 and 2). The final identified system using both steady state and dynamic data generated from Model 1 appears in Table 7.

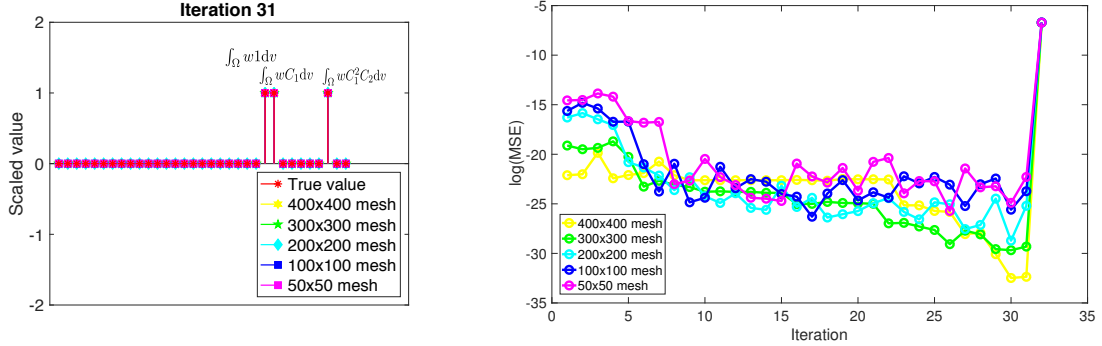


Figure 20: Inferred operators for C_1 (left panel) using noise-free data generated from Model 1 at steady state, and the loss (right panel) at each iteration. The identified coefficients of active operators are scaled by their true values. The algorithm converges at iteration 31, beyond which the loss increases dramatically if any more active operators are eliminated.

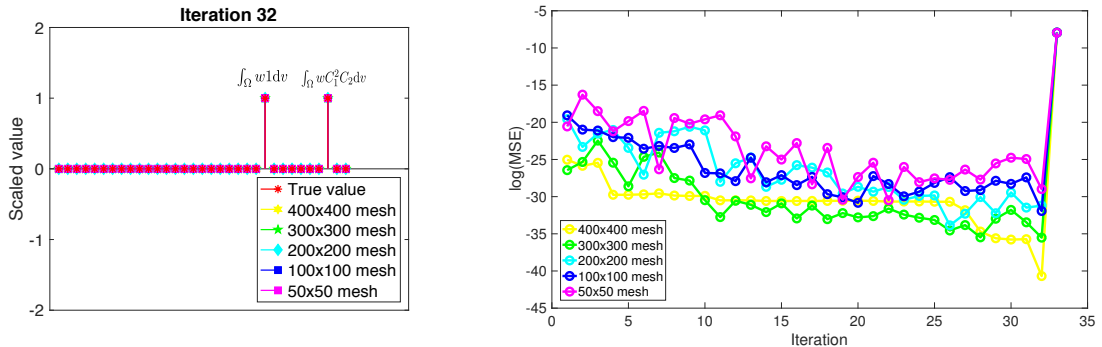


Figure 21: Inferred operators for C_2 (left panel) using noise-free data generated from Model 1 at steady state, and the loss (right panel) at each iteration. The identified coefficients of active operators are scaled by their true values. The algorithm converges at iteration 32, beyond which the loss increases dramatically if any more active operators are eliminated.

Cahn-Hilliard equations behave differently from the diffusion-reaction equations in terms of how they attain steady state. After the initial fast spinodal decomposition, Ostwald ripening occurs, in which the larger particles grow slowly at the expense of smaller ones. As a result, following the initial spinodal decomposition, the evolution of concentrations is extremely slow (See Figure 22),

Snapshot size	400×400	300×300	200×200	100×100	50×50
θ_{D_1}	0.9998	0.9998	1.001	0.995	0.994
θ_{D_2}	39.95	40.01	40.02	39.72	39.23

Table 3: The identified scaling factor for governing equation of C_1 and C_2 using data generated from Model 1 with different sizes of snapshots. The true values are $\theta_{D_1} = 1$ and $\theta_{D_2} = 40$.

and thus the system is at near-steady state:

$$\nabla \cdot (M_1 \nabla \mu_1) \approx 0 \quad (68)$$

$$\nabla \cdot (M_2 \nabla \mu_2) \approx 0 \quad (69)$$

We again find the sets of consistent operators using Algorithm 3, and they appear in Figure 23.

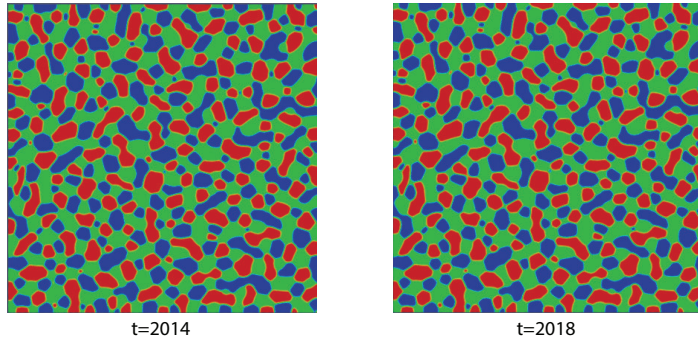


Figure 22: C_1 concentrations at closely spaced time instants with Model 2. The Cahn-Hilliard equations evolve very slowly in the Ostwald ripening stage following the initial spinodal decomposition. The system is at near-steady state around $t = 2018$.

Unlike the manner in which Algorithm 3 played out for the steady state diffusion-reaction equations, the choice of target operators that are common to both governing equations in the system does not result in convergence to a single set of operators. This is because the two equations in Model 2 have more than a single operator that is unique to each of them. When these are chosen as targets, Algorithm 3 correctly identifies two distinct sets of operators, each being self-consistent. These sets represent the two Cahn-Hilliard equations (68) and (69). Also as with the diffusion-reaction equations at steady state, the choice of inactive operators as targets yields inconsistent sets of inferred operators as shown in Figure 24.

In the following we choose the two biharmonic operators, $\nabla^4 C_1$ and $\nabla^4 C_2$, as the targets and

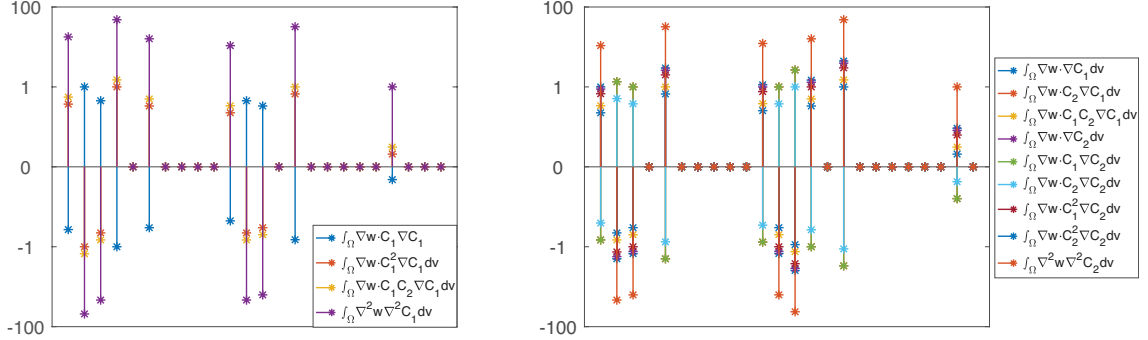


Figure 23: Two sets of consistently inferred operators starting with different targets and using data generated from Model 2 at steady state. The coefficient values have been plotted on the logarithmic scale in order to make them discernible across orders of magnitude. The two consistent sets consist of the operators, from left to right, appearing on the right hand-side of Equations (57) and (58), and differ only by a scaling factor. The two consistent sets are labelled by the target operator shown in the legends of the two sub-plots.

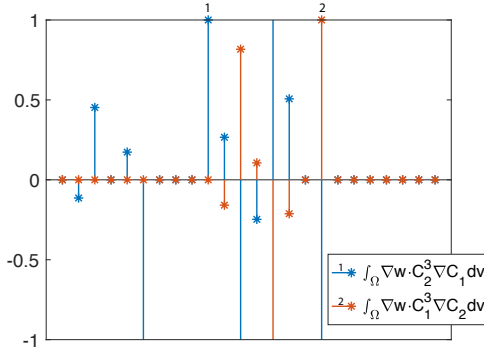


Figure 24: One example of inconsistently inferred sets of operators, shown in different color of stems and leaves, starting with different targets using data generated from Model 2 at steady state. Choosing $\int_{\Omega} \nabla w \cdot C_1^3 \nabla C_1 dv$, labelled by 1, as target, $\int_{\Omega} \nabla w \cdot C_2 \nabla C_1 dv$, labelled by 2, is inferred as being active, but not *vice versa*. In fact, both operators are inactive in this system.

infer the remaining operators, $\bar{\chi}$:

$$\nabla^4 C_1 = \frac{1}{\theta_{k_1}} \bar{\chi} \cdot \bar{\theta} \quad (70)$$

$$\nabla^4 C_2 = \frac{1}{\theta_{k_2}} \bar{\chi} \cdot \bar{\theta}. \quad (71)$$

Very accurate results are obtained from data without noise, even if the snapshots are small as shown in Figures 25 and 26. Following identification of the two consistent sets of operators at steady state by Algorithm 3, the scaling factors, θ_{k_1} and θ_{k_2} in Equations (70) and (71), i.e. the coefficients for biharmonic operators, are correctly identified using Stage 2 of VSI with dynamic data and weighting function $w^h = C_1^h$ and $w^h = C_2^h$. These results appear in Table 4. The final VSI results using both steady state and dynamic data generated from Model 2 appears in Table 8.

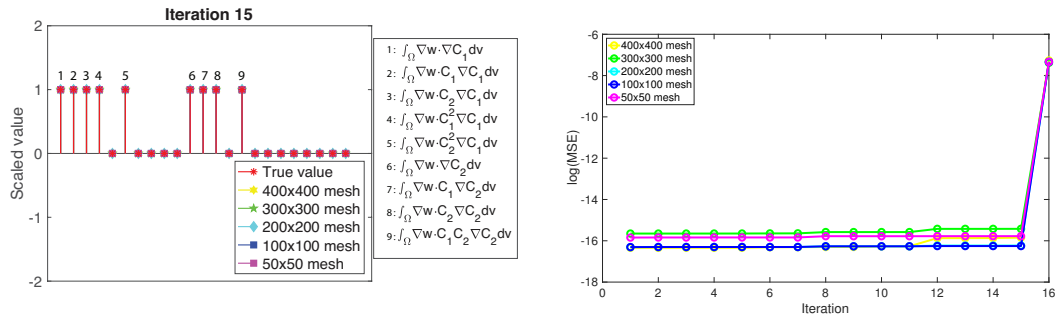


Figure 25: Inferred operators for C_1 (left panel) using data generated from Model 2 at steady state, and the loss (right panel) at each iteration. The identified coefficients of active operators are scaled by their true values. The algorithm converges at iteration 15, beyond which the loss increases dramatically if any more active operators are eliminated.

Snapshot size	400×400	300×300	200×200	100×100	50×50
θ_{k_1}	0.978	0.898	0.922	0.86	0.846
θ_{k_2}	0.994	0.91	0.91	1.08	1.27

Table 4: The identified scaling factor for governing equation of C_1 and C_2 using data generated from Model 2 with different size of snapshots. The true value is 1 for both coefficients.

We remark that we have previously studied the effect of noise on VSI with full-field data [27]. Those results apply in entirety to VSI with steady state data as presented in this section.

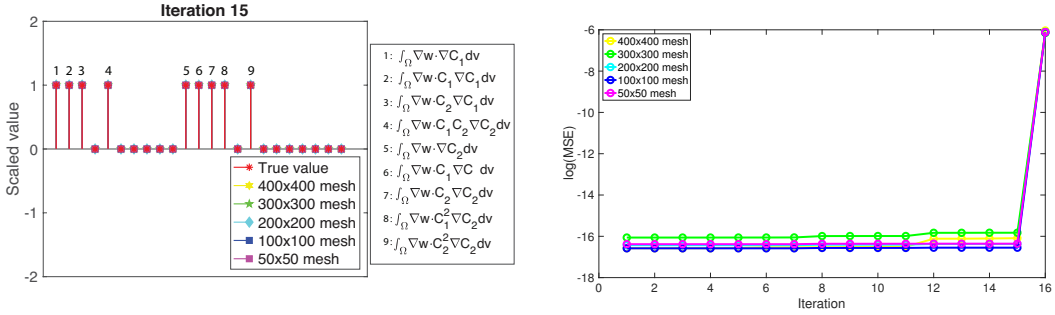


Figure 26: Inferred operators for C_2 (left panel) using data generated from Model 2 at steady state, and the loss (right panel) at each iteration. The identified coefficients of active operators are scaled by their true values. The algorithm converges at iteration 15, beyond which the loss increases dramatically if any more active operators are eliminated.

4 Discussion and conclusions

The development of patterns in many physical phenomena is governed by a range of spatio-temporal PDEs. It is compelling to attempt to discover the analytic forms of these PDEs from data, because doing so immediately provides insight to the governing physics. System identification has been explored using the strong form [26, 28, 29, 37, 38] and the weak form [27] of the PDEs as discussed in the Introduction. These techniques, however all need data that are spatially overlapping at distinct times in order to construct the time derivative operator. However, in materials physics in particular, the combination of processing and microscopy techniques results in datasets that are discordant with the PDE description of temporal evolution at fixed spatial locations. Microscopy data are only obtained over subsets of the entire domains, and the measured data at distinct times typically come from different experiments or specimens. This property of the datasets hinders the use of system identification methods including SINDy and VSI. While Bayesian methods, also discussed in the Introduction, are more flexible in working with such datasets, they require many forward solutions of the PDEs. Their computational expense makes it challenging to determine operators in PDEs from a comprehensive library of candidates.

For development of patterns in materials physics, dynamic information can be inferred from data collected from different specimens and at different times, because of the global statistical similarity of the patterns (See Figures 1 and 4). Many statistical measurements, e.g. the moments of the concentration fields, can be well approximated using such data. Moments can be recovered by specific choices of weighting function that allow a two-stage approach to separate the identification of algebraic and differential operators. VSI can thus be extended to incorporate spatially unrelated (and non-overlapping) and sparse information. Data available from larger snapshots; i.e., larger subsets of the entire domain yield better approximations of the global quantities as discussed in Section 2.5.2. The poor approximations using small snapshots pose challenges to system identi-

fication, resulting in inactive operators being incorrectly identified (e.g., Figure 12). In practice, however, we may have much higher resolution of data in experiments than the smallest snapshots of 50×50 that were assumed here. This opens a door to improving the success of our methods.

We had already shown [27] that, given data from a few temporal snapshots but with high spatial resolution, VSI can pinpoint the complete governing equations of dynamical systems. Here, we have further leveraged steady state data that already provide information about most of the operators in the system, up to scaling factors corresponding to kinetic coefficients such as diffusivities and mobilities that determine the time scales. In Section 3.2, we demonstrated that, using data at steady state, we could identify all the operators in the PDEs up to a scaling factor. Without prior knowledge it is challenging to choose relevant operators to be the targets in our methods at steady state. However, by examining the consistency of the inferred operators using different candidates as the target, we were able to identify all the governing equations at steady state. The associated Confirmation Test of Consistency with Operator Suppression has flavors of traditional approaches such as cross validation but is a mathematically stronger guarantee in that it confirms the identified result without prior knowledge or additional data. Identification of the single unknown in the original dynamic equations is then reduced to a straightforward exercise with two-stage VSI, which we have described for algebraic and differential operators, respectively. Thus, in cases wherein steady state (or near-steady state) data are available, they serve as a “zeroth” step to be followed by only one of the stages that have been laid out for dynamic data in Section 2. If the dynamics remain far from steady state, the two-stage VSI is still applicable, given snapshots at sufficiently many time instants.

Acknowledgements

We acknowledge the support of Toyota Research Institute, Award #849910, “Computational framework for data-driven, predictive, multi-scale and multi-physics modeling of battery materials” (ZW and KG). Additional support: This material is based upon work supported by the Defense Advanced Research Projects Agency (DARPA) under Agreement No. HR0011199002, “Artificial Intelligence guided multi-scale multi-physics framework for discovering complex emergent materials phenomena” (ZW, XH and KG).

Appendix

mesh size	results
400×400	$\int_{\Omega} w_1 \frac{\partial C_1}{\partial t} dv = \int_{\Omega} -1.0252 \nabla w_1 \cdot \nabla C_1 dv + \int_{\Omega} w_1 (0.1 - C_1 + 1C_1^2 C_2) dv$ $\int_{\Omega} w_2 \frac{\partial C_2}{\partial t} dv = \int_{\Omega} -42.0655 \nabla w_2 \cdot \nabla C_2 dv + \int_{\Omega} w_2 (0.9 - 1C_1^2 C_2) dv$
300×300	$\int_{\Omega} w_1 \frac{\partial C_1}{\partial t} dv = \int_{\Omega} -0.9644 \nabla w_1 \cdot \nabla C_1 dv + \int_{\Omega} w_1 (0.0987 - 0.9992 C_1 + 1.00002 C_1^2 C_2) dv$ $\int_{\Omega} w_2 \frac{\partial C_2}{\partial t} dv = \int_{\Omega} -42.2344 \nabla w_2 \cdot \nabla C_2 dv + \int_{\Omega} w_2 (0.89982 - 0.9998 C_1^2 C_2) dv$
200×200	$\int_{\Omega} w_1 \frac{\partial C_1}{\partial t} dv = \int_{\Omega} -1.0212 \nabla w_1 \cdot \nabla C_1 dv + \int_{\Omega} w_1 (0.0993 - 1.0007 C_1 + 1.0017 C_1^2 C_2) dv$ $\int_{\Omega} w_2 \frac{\partial C_2}{\partial t} dv = \int_{\Omega} -42.1083 \nabla w_2 \cdot \nabla C_2 dv + \int_{\Omega} w_2 (0.89982 - 0.9998 C_1^2 C_2) dv$
100×100	$\int_{\Omega} w_1 \frac{\partial C_1}{\partial t} dv = \int_{\Omega} -0.7576 \nabla w_1 \cdot \nabla C_1 dv + \int_{\Omega} w_1 (0.1035 - 0.9954 C_1 + 0.9908 C_1^2 C_2) dv$ $\int_{\Omega} w_2 \frac{\partial C_2}{\partial t} dv = \int_{\Omega} 2.77 \nabla w_2 \cdot C_1^2 \nabla C_1 dv + \int_{\Omega} w_2 (0.9019 - 1.0026 C_1^2 C_2) dv$
50×50	$\int_{\Omega} w_1 \frac{\partial C_1}{\partial t} dv = \int_{\Omega} -0.8154 \nabla w_1 \cdot \nabla C_1 dv + \int_{\Omega} w_1 (0.1035 - 0.9889 C_1 + 0.9804 C_1^2 C_2) dv$ $\int_{\Omega} w_2 \frac{\partial C_2}{\partial t} dv = \int_{\Omega} 4 \nabla w_2 \cdot C_1^2 C_2 \nabla C_1 dv + \int_{\Omega} w_2 (0.9075 - 1.01 C_1^2 C_2) dv$

Table 5: Results using noise-free dynamic data generated from Model 1.

mesh size	results
400×400	$\int_{\Omega} w_1 \frac{\partial C_1}{\partial t} dv = \int_{\Omega} -1.0675 \nabla w_1 \cdot \nabla C_1 dv + \int_{\Omega} w_1 (0.0937 - 0.9876 C_1 + 0.9912 C_1^2 C_2) dv$ $\int_{\Omega} w_2 \frac{\partial C_2}{\partial t} dv = \int_{\Omega} -42.2038 \nabla w_2 \cdot \nabla C_2 dv + \int_{\Omega} w_2 (0.8662 - 0.9661 C_1^2 C_2) dv$
300×300	$\int_{\Omega} w_1 \frac{\partial C_1}{\partial t} dv = \int_{\Omega} -1.1105 \nabla w_1 \cdot \nabla C_1 dv + \int_{\Omega} w_1 (0.0941 - 0.9876 C_1 + 0.991 C_1^2 C_2) dv$ $\int_{\Omega} w_2 \frac{\partial C_2}{\partial t} dv = \int_{\Omega} -42.0852 \nabla w_2 \cdot \nabla C_2 dv + \int_{\Omega} w_2 (0.8668 - 0.9663 C_1^2 C_2) dv$
200×200	$\int_{\Omega} w_1 \frac{\partial C_1}{\partial t} dv = \int_{\Omega} -1.2102 \nabla w_1 \cdot \nabla C_1 dv + \int_{\Omega} w_1 (0.0944 - 0.9882 C_1 + 0.9912 C_1^2 C_2) dv$ $\int_{\Omega} w_2 \frac{\partial C_2}{\partial t} dv = \int_{\Omega} -55.257 \nabla w_2 \cdot C_2 \nabla C_2 dv + \int_{\Omega} w_2 (0.8662 - 0.9651 C_1^2 C_2) dv$
100×100	$\int_{\Omega} w_1 \frac{\partial C_1}{\partial t} dv = \int_{\Omega} -1.1579 \nabla w_1 \cdot \nabla C_1 dv + \int_{\Omega} w_1 (0.0895 - 0.9897 C_1 + 0.9992 C_1^2 C_2) dv$ $\int_{\Omega} w_2 \frac{\partial C_2}{\partial t} dv = \int_{\Omega} -54.989 \nabla w_2 \cdot C_2 \nabla C_2 dv + \int_{\Omega} w_2 (-0.8682 - 0.967 C_1^2 C_2) dv$
50×50	$\int_{\Omega} w_1 \frac{\partial C_1}{\partial t} dv = \int_{\Omega} -0.8997 \nabla w_1 \cdot \nabla C_1 dv + \int_{\Omega} w_1 (0.0836 - 0.9826 C_1 + 0.9973 C_1^2 C_2) dv$ $\int_{\Omega} w_2 \frac{\partial C_2}{\partial t} dv = \int_{\Omega} 7.93 \nabla w_2 \cdot C_1 \nabla C_1 dv + \int_{\Omega} w_2 (-0.8733 - 0.9726 C_1^2 C_2) dv$

Table 6: Results using noisy dynamic data generated from Model 1.

mesh size	results
400×400	$\int_{\Omega} w_1 \frac{\partial C_1}{\partial t} dv = \int_{\Omega} -0.9998 \nabla w_1 \cdot \nabla C_1 dv + \int_{\Omega} w_1 (0.1 - 0.9998 C_1 + 0.9998 C_1^2 C_2) dv$ $\int_{\Omega} w_2 \frac{\partial C_2}{\partial t} dv = \int_{\Omega} -39.95 \nabla w_2 \cdot \nabla C_2 + \int_{\Omega} w_2 (0.8989 - 0.9987 C_1^2 C_2) dv$
300×300	$\int_{\Omega} w_1 \frac{\partial C_1}{\partial t} dv = \int_{\Omega} -1.001 \nabla w_1 \cdot \nabla C_1 dv + \int_{\Omega} w_1 (0.1 - 0.9998 C_1 + 0.9998 C_1^2 C_2) dv$ $\int_{\Omega} w_2 \frac{\partial C_2}{\partial t} dv = \int_{\Omega} -40.01 \nabla w_2 \cdot \nabla C_2 + \int_{\Omega} w_2 (0.9002 - 1.0002 C_1^2 C_2) dv$
200×200	$\int_{\Omega} w_1 \frac{\partial C_1}{\partial t} dv = \int_{\Omega} -0.995 \nabla w_1 \cdot \nabla C_1 dv + \int_{\Omega} w_1 (0.1001 - 1.001 C_1 + 1.001 C_1^2 C_2) dv$ $\int_{\Omega} w_2 \frac{\partial C_2}{\partial t} dv = \int_{\Omega} -40.02 \nabla w_2 \cdot \nabla C_2 + \int_{\Omega} w_2 (0.9005 - 1.005 C_1^2 C_2) dv$
100×100	$\int_{\Omega} w_1 \frac{\partial C_1}{\partial t} dv = \int_{\Omega} -0.0994 \nabla w_1 \cdot \nabla C_1 dv + \int_{\Omega} w_1 (0.0995 - 0.995 C_1 + 0.995 C_1^2 C_2) dv$ $\int_{\Omega} w_2 \frac{\partial C_2}{\partial t} dv = \int_{\Omega} -39.72 \nabla w_2 \cdot \nabla C_2 + \int_{\Omega} w_2 (-0.8937 - 0.993 C_1^2 C_2) dv$
50×50	$\int_{\Omega} w_1 \frac{\partial C_1}{\partial t} dv = \int_{\Omega} -0.0994 \nabla w_1 \cdot \nabla C_1 dv + \int_{\Omega} w_1 (0.0994 - 0.994 C_1 + 0.994 C_1^2 C_2) dv$ $\int_{\Omega} w_2 \frac{\partial C_2}{\partial t} dv = \int_{\Omega} -39.23 \nabla w_2 \cdot \nabla C_2 + \int_{\Omega} w_2 (-0.8827 - 0.9807 C_1^2 C_2) dv$

Table 7: Results using steady state and dynamic data generated from Model 1.

mesh size	results
400 × 400	$\int_{\Omega} w_1 \frac{\partial C_1}{\partial t} dv = \int_{\Omega} \nabla w_1 \cdot (-17.417 + 46.9146C_1 + 21.114C_2 - 46.91C_1^2 - 15.64C_2^2) \nabla C_1 dv$ $+ \int_{\Omega} \nabla w_2 \nabla \cdot (-10.55 + 21.11C_1 + 15.64C_2 - 31.177C_1C_2) \nabla C_2 dv + \int_{\Omega} -0.978 \nabla^2 w_1 \nabla^2 C_1 dv$ $\int_{\Omega} w_2 \frac{\partial C_2}{\partial t} dv = \int_{\Omega} \nabla w_2 \cdot (-10.73 + 21.46C_1 + 15.9C_2 - 31.79C_1C_2) \nabla C_1 dv$ $+ \int_{\Omega} \nabla w_2 \nabla \cdot (-12.13 + 15.88C_1 + 42.12C_2 - 15.88C_1^2 - 47.68C_2^2) \nabla^2 C_2 dv + \int_{\Omega} -0.994 \nabla^2 w_2 \nabla^2 C_2 dv$
300 × 300	$\int_{\Omega} w_1 \frac{\partial C_1}{\partial t} dv = \int_{\Omega} \nabla w_1 \cdot (-15.992 + 43.08C_1 + 19.38C_2 - 43.08C_1^2 - 14.364C_2^2) \nabla C_1 dv$ $+ \int_{\Omega} \nabla w_2 \nabla \cdot (-9.69 + 19.38C_1 + 14.36C_2 - 28.71C_1C_2) \nabla C_2 dv + \int_{\Omega} -0.898 \nabla^2 w_1 \nabla^2 C_1 dv$ $\int_{\Omega} w_2 \frac{\partial C_2}{\partial t} dv = \int_{\Omega} \nabla w_2 \cdot (-9.82 + 19.65C_1 + 14.55C_2 - 29.11C_1C_2) \nabla C_1 dv$ $+ \int_{\Omega} \nabla w_2 \nabla \cdot (-11.11 + 14.54C_1 + 38.56C_2 - 14.54C_1^2 - 43.66C_2^2) \nabla^2 C_2 dv + \int_{\Omega} -0.91 \nabla^2 w_2 \nabla^2 C_2 dv$
200 × 200	$\int_{\Omega} w_1 \frac{\partial C_1}{\partial t} dv = \int_{\Omega} \nabla w_1 \cdot (-16.42 + 44.23C_1 + 19.9C_2 - 44.23C_1^2 - 14.74C_2^2) \nabla C_1 dv$ $+ \int_{\Omega} \nabla w_2 \nabla \cdot (-9.95 + 19.9C_1 + 14.74C_2 - 29.48C_1C_2) \nabla C_2 dv + \int_{\Omega} -0.86 \nabla^2 w_1 \nabla^2 C_1 dv$ $\int_{\Omega} w_2 \frac{\partial C_2}{\partial t} dv = \int_{\Omega} \nabla w_2 \cdot (-9.82 + 19.65C_1 + 14.55C_2 - 29.11C_1C_2) \nabla C_1 dv$ $+ \int_{\Omega} \nabla w_2 \nabla \cdot (-11.1 + 14.54C_1 + 38.56C_2 - 14.53C_1^2 - 43.66C_2^2) \nabla^2 C_2 dv + \int_{\Omega} -0.91 \nabla^2 w_2 \nabla^2 C_2 dv$
100 × 100	$\int_{\Omega} w_1 \frac{\partial C_1}{\partial t} dv = \int_{\Omega} \nabla w_1 \cdot (-15.31 + 41.25C_1 + 18.57C_2 - 41.25C_1^2 - 13.76C_2^2) \nabla C_1 dv$ $+ \int_{\Omega} \nabla w_2 \nabla \cdot (-9.27 + 18.55C_1 + 13.74C_2 - 27.48C_1C_2) \nabla C_2 dv + \int_{\Omega} -0.86 \nabla^2 w_1 \nabla^2 C_1 dv$ $\int_{\Omega} w_2 \frac{\partial C_2}{\partial t} dv = \int_{\Omega} \nabla w_2 \cdot (-11.66 + 23.32C_1 + 17.27C_2 - 34.55C_1C_2) \nabla C_1 dv$ $+ \int_{\Omega} \nabla w_2 \nabla \cdot (-13.18 + 17.24C_1 + 45.76C_2 - 17.24C_1^2 - 51.81C_2^2) \nabla^2 C_2 dv + \int_{\Omega} -1.08 \nabla^2 w_2 \nabla^2 C_2 dv$
50 × 50	$\int_{\Omega} w_1 \frac{\partial C_1}{\partial t} dv = \int_{\Omega} \nabla w_1 \cdot (-15.06 + 40.57C_1 + 18.28C_2 - 40.57C_1^2 - 13.55C_2^2) \nabla C_1 dv$ $+ \int_{\Omega} \nabla w_2 \nabla \cdot (-9.11 + 18.23C_1 + 13.5C_2 - 27C_1C_2) \nabla C_2 dv + \int_{\Omega} -0.846 \nabla^2 w_1 \nabla^2 C_1 dv$ $\int_{\Omega} w_2 \frac{\partial C_2}{\partial t} dv = \int_{\Omega} \nabla w_2 \cdot (-13.71 + 27.42C_1 + 20.31C_2 - 40.62C_1C_2) \nabla C_1 dv$ $+ \int_{\Omega} \nabla w_2 \nabla \cdot (-15.48 + 20.23C_1 + 53.81C_2 - 20.23C_1^2 - 60.94C_2^2) \nabla^2 C_2 dv + \int_{\Omega} -1.27 \nabla^2 w_2 \nabla^2 C_2 dv$

Table 8: Results using steady state and dynamic data generated from Model 2.

References

1. T. Jiang, S. Rudraraju, A. Roy, A. Van der Ven, K. Garikipati, and M. L. Falk. Multi-physics simulations of lithiation-induced stress in litio electrode particles. *J. Phys. Chem. C*, 120, 2016.
2. S. Rudraraju, A. Van der Ven, and K. Garikipati. Mechano-chemical spinodal decomposition: A phenomenological theory of phase transformations in multi-component crystalline solids. *Nature Computational Materials*, 2, 2016.
3. G.H. Teichert, S. Rudraraju, and K. Garikipati. A variational treatment of material configurations with application to interface motion and microstructural evolution. *Journal of the Mechanics and Physics of Solids*, 99, 2017.
4. J. W. Cahn and J. E. Hilliard. Free energy of a nonuniform system. i interfacial energy. *J. Chem. Phys.*, 28, 1958.
5. A. M. Turing. The chemical basis of morphogenesis. *Phil. Trans. Roy. Soc. Lond. Ser. B.*, 237, 1952.
6. A. Gierer and H. Meinhardt. A theory of biological pattern formation. *Kybernetik*, 12, 1972.
7. J. D. Murray. On pattern formation mechanisms for lepidopteran wing patterns and mammalian coat markings. *Phil. Trans. Roy. Soc. Lond. Ser. B*, 295, 1981.
8. R. Dillon, P. K. Maini, and H. G. Othmer. Pattern formation in generalized turing systems i: Steady-state patterns in systems with mixed boundary conditions. *J. Math. Biol.*, 32, 1994.
9. R. A. Barrio, C. Varea, and J. L. Aragon. A two-dimensional numerical study of spatial pattern formation in interacting turing systems. *Bull. Math. Biol.*, 61, 1999.
10. R. A. Barrio, R. E. Baker, B. Vaughan, K. Tribuzy, M. R. de Carvalho, Rodney Bassanezi, and P. K. Maini. Modeling the skin pattern of fishes. *Phys. Rev. E*, 79, 2009.
11. Philip K. Maini, Thomas E. Woolley, Ruth E. Baker, Eamonn A. Gaffney, and S. Seirin Lee. Turing's model for biological pattern formation and the robustness problem. *Interface Focus*, 2(4):487–496, 2012. doi: 10.1098/rsfs.2011.0113.
12. F. Spill, P. Guerrero, T. Alarcon, P. K. Maini, and H. Byrne. Hybrid approaches for multiple-species stochastic reaction-diffusion models. *J. Comput. Phys.*, 299, 2015.
13. K. Korvasová, E. A. Gaffney, P. K. Maini, M. A. Ferreira, and V. Klika. Investigating the turing conditions for diffusion-driven instability in the presence of a binding immobile substrate. *J. Theor. Biol.*, 367, 2015.

14. K. Garikipati. Perspectives on the mathematics of biological patterning and morphogenesis. *J. Mech. Phys. Solids.*, 99, 2017.
15. S. M. Wise, J. S. Lowengrub, H. B. Frieboes, and V. Cristini. Three-dimensional multispecies nonlinear tumor growth–model and numerical method. *J. Theor. Biol.*, 253, 2008.
16. V. Cristini, X. Li, J. S. Lowengrub, and S. M. Wise. Nonlinear simulations of solid tumor growth using a mixture model: invasion and branching. *J. Math. Biol.*, 58, 2009.
17. J. S. Lowengrub, H. B. Frieboes, F. Jin, Y-L. Chuang, X. Li, Macklin, S. M. Wise, and V. Cristini. Nonlinear modelling of cancer: bridging the gap between cells and tumours. *Nonlinearity*, 23, 2010.
18. J. S. Lowengrub, A. Rätz, and A. Voigt. Phase-field modeling of the dynamics of multicomponent vesicles: Spinodal decomposition, coarsening, budding, and fission. *Phys. Rev. E*, 79, 2009.
19. G. Vilanova, I. Colominas, and H. Gomez. Capillary networks in tumor angiogenesis: From discrete endothelial cells to phase-field averaged descriptions via isogeometric analysis. *Num. Meth. Biomed. Eng.*, 29, 2013.
20. G. Vilanova, I. Colominas, and H. Gomez. Coupling of discrete random walks and continuous modeling for three-dimensional tumor-induced angiogenesis. *Comput. Mech.*, 53, 2014.
21. J. T. Oden, A. Hawkins, and S. Prudhomme. General diffuse-interface theories and an approach to predictive tumor growth modeling. *Math. Mod. Meth. App. Sci.*, 20, 2010.
22. J. Xu, G. Vilanova, and H. Gomez. A mathematical model coupling tumor growth and angiogenesis. *PLoS ONE*, 11, 2016.
23. R. HilleRisLambers, M. Rietkerk, F. van den Bosch, H.H.T. Prins, and H. de Kroon. Vegetation pattern formation in semi-arid grazing systems. *Ecol.*, 82:50–61, 2001.
24. M. Rietkerk and J. van de Koppel. Regular pattern formation in real ecosystems. *Trends Ecol. Evol.*, 23:169–175, 2008.
25. Steve Brooks, Andrew Gelman, Galin Jones, and Xiao-Li Meng, editors. *Handbook of Markov Chain Monte Carlo*. Chapman and Hall/CRC, 2011. ISBN 978-1-4200-7941-8. doi: 10.1201/b10905.
26. S. L. Brunton, J. L. Proctor, and J. N. Kutz. Discovering governing equations from data by sparse identification of nonlinear dynamical systems. *Proc. Natl. Acad. Sci.*, 113, 2016.

27. Z. Wang, X. Huan, and K. Garikipati. Variational system identification of the partial differential equations governing the physics of pattern-formation: Inference under varying fidelity and noise. *Computer Methods in Applied Mechanics and Engineering*, 356:44 – 74, 2019. ISSN 0045-7825. doi: <https://doi.org/10.1016/j.cma.2019.07.007>.
28. N. M. Mangan, S. L. Brunton, J. L. Proctor, and J. N. Kutz. Inferring biological networks by sparse identification of nonlinear dynamics. *IEEE Trans. Mol. Biol. Multi-Scale Commun.*, 2, 2016.
29. S. H. Rudy, S. L. Brunton, J. L. Proctor, and J. N. Kutz. Data-driven discovery of partial differential equations. *Sci. Adv.*, 3, 2017.
30. M. Raissi, P. Perdikaris, and G.E. Karniadakis. Physics-informed neural networks: A deep learning framework for solving forward and inverse problems involving nonlinear partial differential equations. *J. Comput. Phys.*, 378, 2019.
31. Z. Wang, B. Wu X. Huan, and K. Garikipati. A perspective on regression and bayesian approaches for system identification of pattern formation dynamics. *arXiv:2001.05646*, 2020.
32. J. Cottrell, T. Hughes, and Y. Bazilevs. Isogeometric analysis: Toward integration of cad and fea. *Wiley, Chichester*, 2009.
33. Emmanuel J. Candès, Justin Romberg, and Terence Tao. Robust Uncertainty Principles: Exact Signal Reconstruction From Highly Incomplete Frequency Information. *IEEE Transactions on Information Theory*, 52(2):489–509, 2006. ISSN 0018-9448. doi: 10.1109/TIT.2005.862083.
34. David L. Donoho. Compressed sensing. *IEEE Transactions on Information Theory*, 52(4): 1289–1306, 2006. ISSN 00189448. doi: 10.1109/TIT.2006.871582.
35. G. James, D. Witten, T. Hastie, and R. Tibshirani. An introduction to statistical learning. *Springer New York, Inc., New York, NY, USA.*, 2013.
36. J. Schnakenberg. Network theory of microscopic and macroscopic behavior of master equation systems. *Rev. Mod. Phys.*, 48, 1976.
37. M. Schmidt and H. Lipson. Distilling free-form natural laws from experimental data. *Science*, 03, 2009.
38. M. D Schmidt, R. R Vallabhajosyula, J. W Jenkins, J. E Hood, A. S Soni, J P Wikswo, and H. Lipson. Automated refinement and inference of analytical models for metabolic networks. *Phys. Biol.*, 8, 2011.